Theses and Dissertations--Physics and Astronomy

Physics and Astronomy

2013

Voltage Modulated Infrared Reflectance Study of Soluble Organic Semiconductors in Thin Film Transistors

Emily Geraldine Bittle
University of Kentucky, egbittle@gmail.com

Recommended Citation

Bittle, Emily Geraldine, "Voltage Modulated Infrared Reflectance Study of Soluble Organic Semiconductors in Thin Film Transistors" (2013). *Theses and Dissertations--Physics and Astronomy*. 10.
https://uknowledge.uky.edu/physastron_etds/10

STUDENT AGREEMENT:

I represent that my thesis or dissertation and abstract are my original work. Proper attribution has been given to all outside sources. I understand that I am solely responsible for obtaining any needed copyright permissions. I have obtained and attached hereto needed written permission statements(s) from the owner(s) of each third-party copyrighted matter to be included in my work, allowing electronic distribution (if such use is not permitted by the fair use doctrine).

I hereby grant to The University of Kentucky and its agents the non-exclusive license to archive and make accessible my work in whole or in part in all forms of media, now or hereafter known. I agree that the document mentioned above may be made available immediately for worldwide access unless a preapproved embargo applies.

I retain all other ownership rights to the copyright of my work. I also retain the right to use in future works (such as articles or books) all or part of my work. I understand that I am free to register the copyright to my work.

REVIEW, APPROVAL AND ACCEPTANCE

The document mentioned above has been reviewed and accepted by the student’s advisor, on behalf of the advisory committee, and by the Director of Graduate Studies (DGS), on behalf of the program; we verify that this is the final, approved version of the student’s dissertation including all changes required by the advisory committee. The undersigned agree to abide by the statements above.

Emily Geraldine Bittle, Student

Dr. Joseph W. Brill, Major Professor

Dr. Timothy Gorringe, Director of Graduate Studies

VOLTAGE MODULATED INFRARED REFLECTANCE STUDY OF SOLUBLE ORGANIC SEMICONDUCTORS IN THIN FILM TRANSISTORS

DISSERTATION

A dissertation submitted in partial
fulfillment of the requirements for
the degree of Doctor of Philosophy
in the College of Arts and Sciences
at the University of Kentucky

By
Emily Geraldine Bittle
Lexington, Kentucky

Director: Dr. Joseph W. Brill, Professor of Physics and Astronomy
Lexington, Kentucky 2013

ABSTRACT OF DISSERTATION

VOLTAGE MODULATED INFRARED REFLECTANCE STUDY OF SOLUBLE ORGANIC SEMICONDUCTORS IN THIN FILM TRANSISTORS

Soluble organic semiconductors have attracted interest due to their potential in making flexible and cheap electronics. Though their use is being implemented in electronics today, the conduction mechanism is still under investigation. In order to study the charge transport, this study examines the position, voltage, and frequency dependence of charge induced changes in far infrared absorption in soluble organic semiconductors in thin-film transistor structures. Measurements are compared to a simple model of a one-dimensional conductor which gives insight into the charge distribution and timing in devices. Main results of the study are dynamic measurements of charge taken by varying the frequency of the applied gate voltage while observing signal at one position within the transistor; mobility values obtained from a comparison to the one-dimensional model compare well with standard current-voltage measurements. Two small molecule soluble organic semiconductors were studied: 6,13 bis(triisopropylsilylethynyl)-pentacene and fluorinated 5,11 bis(triethylsilylethynyl) anthradithiophene.

KEYWORDS: organic semiconductors, infrared reflectance, organic thin film transistors, electro-optics, mobility

Author's Signature: Emily Geraldine Bittle

Date: March 28, 2013

VOLTAGE MODULATED INFRARED REFLECTANCE STUDY OF SOLUBLE ORGANIC SEMICONDUCTORS IN THIN FILM TRANSISTORS

By

Emily Geraldine Bittle

Joseph W. Brill
Director of thesis

Timothy Gorringe
Director of graduate studies

March 28, 2013

Acknowledgments

No task is completed without the help and encouragement of others, and I extend my gratitude to the people who made this thesis and the completion of my project possible.

The value of a great advisor cannot be overstated for the support and guidance they give throughout the project. I was fortunate to find my advisor Joe Brill and I thank him for his guidance throughout my project and graduate school. Also, I would like to thank my committee for their guidance and support, and for their individual contributions to this project: John Anthony for samples and for arranging my visit to the National Institute of Standards and Technology; to Kwok Wai Ng for helping with early work on transistor structures; and to Joseph Straley for help with calculations that are a part of this thesis.

I would like to thank Gene Baber for all the help he provided; Jim Morris, Charles Tipton and Steve Maynard for machining many of the pieces required for this work; and Greg Porter, Bill Fuqua and Rick Carr for their help building and maintaining the electronics. Thanks to Chuck May and Brian Wajdak at CeNSE for helping me to make and measure thin films. Also, thank you to the staff in the department office for handling the paperwork and administrative details.

Thank you to David Gundlach at NIST for sponsoring my visit, and also to Christina Hacker, Kurt Purnstich, Nayool Shin, Xinran Zhang, Oleg Krillov and others who included me in projects and helped me while there.

Without the friendships I built in graduate school, I would have never stayed in Kentucky long enough to complete my degree. I am honored to have met and struggled through with so many excellent scientists, I especially thank Gretchen Phelps, Erin Peters, Ben Crider, Kristen Thompson, Grant Thompson, John Nichols, and Tongfei Qi.

Finally, thank you to my family, my husband, my husband’s family, and my dance family for their support and encouragement.

TABLE OF CONTENTS

List of Tables

List of Figures

CHAPTER 1 **Background and Theory**

1.1 **Introduction**

Organic semiconductors (OSCs) are a class of organic (composed mainly of carbon and hydrogen) materials that include polymers and small molecules with sp^2 hybridization and delocalized π-electrons. They have attracted attention both in academia and industry for applications which require mechanical flexibility, large area coverage, and inexpensive mass production such as electronic paper, LED displays, and solar cells [1]. Despite progress in applied organic electronics and basic research, the knowledge of fundamental properties in these materials is still limited.

Charge transport in devices, such as field effect transistors, is of particular interest [2]. Device charging is affected by a number of variables, including the fundamental properties of the OSC and interactions with electrical contacts and dielectric materials. To understand charge conduction through organic transistors a number of measurements are being used to probe the local charging, including scanning Kelvin probe microscopy [3,4], electric field generated second harmonic generation [5], and a number of light measurements [6-8].

This thesis covers localized measurements of charge transport in organic field effect transistors (OFETs) using voltage modulated infrared light reflection. Chapter 1 covers the basics of organic thin films transistors and Chapter 2 covers experimental methods and sample preparation. Chapter 3 is an introduction to the basics of the electro-optic measurements on transistors: voltage modulated spectra, voltage dependence of the charge density, and charge distribution measured using voltage modulated infrared reflection. Finally, our main results on dynamic measurements of the charge using infrared reflection, including a unique measurement of the mobility, are discussed in Chapter 4.

1.2 **Soluble Organic Semiconductors**

Materials like pentacene and rubrene are widely studied in OSC research due to their impressive electrical performance. Although these materials are favored in research, the deposition methods required to make thin films (i.e. thermal evaporation) are not suitable to low cost applications in large area, thin film electronics manufacturing. To address this issue, soluble small molecule organic semiconductors have been developed which can be deposited from solution using a variety of techniques, such as drop and spin casting, dip coating [9], inkjet printing [10], and spray coating [11].

Two such materials, developed and synthesized by John Anthony's group at the University of Kentucky, are used in this study. The molecules, shown in Figure 1.1, are 6,13 bis(triisopropylsilylethynyl)-pentacene (TIPS Pn) [12] and fluorinated 5,11 bis(triethylsilylethynyl) anthradithiophene (diF TESADT.) By adding side groups to pentacene and anthradithiophene, these materials become soluble and are able to self assemble into thin film crystals when deposited from common solvents. TIPS Pn can obtain a charge mobility up to 1.3 cm^2/Vs and diF TES ADT up to 1.5 cm^2/Vs for highly crystalline films formed by dip coating [9] which compares favorably with amorphous silicon transistors (on the order of 0.1 cm^2/Vs.)

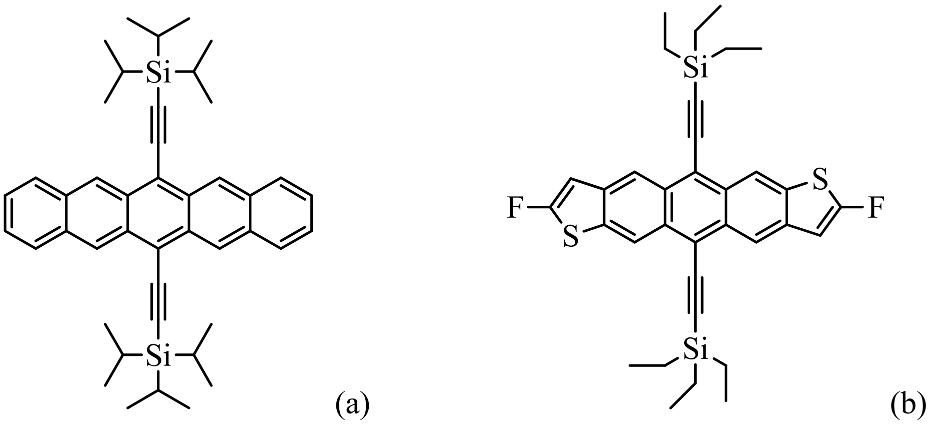

Figure 1.1 Molecular structure of (a) 6,13 bis(triisopropylsilylethynyl)-pentacene (TIPS Pn) and (b) fluorinated 5,11 bis(triethylsilylethynyl) anthradithiophene (diF TES ADT)

The addition of side groups not only increases solubility, but can also be used to control other characteristics of the thin film. Properties such as packing orientation can be controlled to produce films which have better molecular stacking for electrical conduction or decreased degradation in air compared to pentacene or rubrene [13]. The properties of solution processable organic semiconductors make these materials easy to use and ideal for measurement methods which require air exposure.

1.3 **The Field Effect Transistor**

The use of the field effect transistor (FET) structure in fundamental research gives an opportunity to measure the properties of a material, such as the mobility, in a technologically relevant structure: taking into account large charge densities seen in working devices, interactions with the gate dielectric and with electrical contacts [1,2,14]. In our measurements, the FET provides a convenient structure for infrared measurements.

FETs are comprised of a semiconducting material connected at two ends with source and drain electrodes with the center region separated by a thin insulating dielectric from a gate electrode. Different FET configurations are shown in Figure 1.2. Metallic contacts for source and drain are either put above (top contact) or below (bottom contact) the OSC; similarly the FET can be gated from the top or bottom. Doped silicon wafers with oxidized silica layers are often used as substrates that double as gate and dielectric.

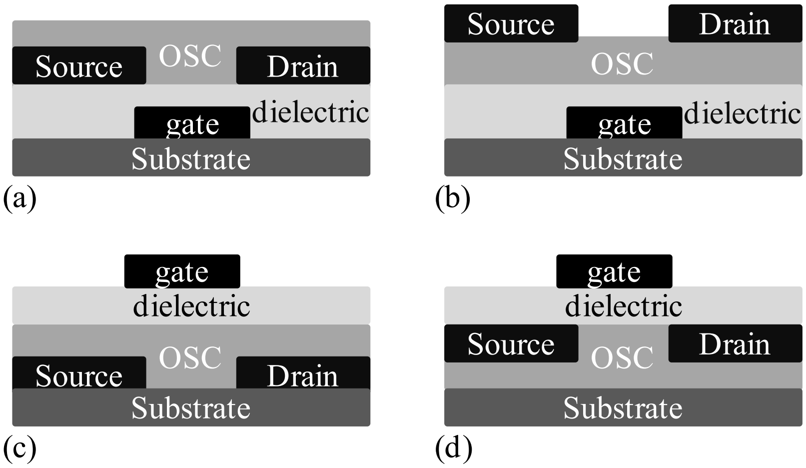

Figure 1.2 Diagrams of configurations for thin film FETs (side view.) (a) bottom contact/ bottom gate, (b) top contact/ bottom gate, (c) bottom contact/ top gate, (d) top contact/ top gate.

When applying voltage to the FET, the source is grounded and voltage is applied to the gate (V_{gs}) and drain (V_{ds}). The density of charge carriers in the conduction channel is modulated by the voltage applied to the gate, this charge then moves parallel to the semiconductor-insulator interface in response to the field imposed by the drain contact. In organic FETs (OFETs) the conduction channel is formed on the interface between the dielectric and the semiconductor by charges originating at the drain and source contacts when a gate voltage is applied.

In an inorganic FET device there are two distinct modes of operation: linear and saturation [15]. The transistor is in linear mode when $V_{ds} < V_{gs}-V_{th}$ and $V_{gs} > V_{th}$ where V_{th} is the threshold gate voltage, which is defined as the point when an inversion layer of charge forms in the semiconductor near the gate. Empirically V_{th} is the gate voltage at which current starts flowing between drain and source contacts through the semiconductor (I_{ds}.) When $V_{ds} = V_{gs} - V_{th}$ the charge nearest to the drain becomes depleted, this effect is known as pinch-off. As V_{ds} gets larger than $V_{gs}-V_{th}$, the pinch-off position moves closer to the source, as shown in Figure 1.2 diagram (b). Past the pinch off value, the current becomes constant and the FET enters saturation mode. The linear and saturation modes adhere to two separate equations:

Linear: $$I_{ds} = \mu_{lin} C_{ox} \frac{W}{L}\left[\left(V_{gs} - V_{th}\right)V_{ds} - \frac{V_{ds}^2}{2}\right]$$ Equation 1.1

Saturation : $$I_{ds} = \mu_{sat} C_{ox} \frac{W}{2L}\left(V_{gs} - V_{th}\right)^2$$ Equation 1.2

where L is the length of the channel, W is the width of the channel, μ is the mobility of the OFET in the linear or saturation modes, and C_{ox} is the capacitance per area for the dielectric.

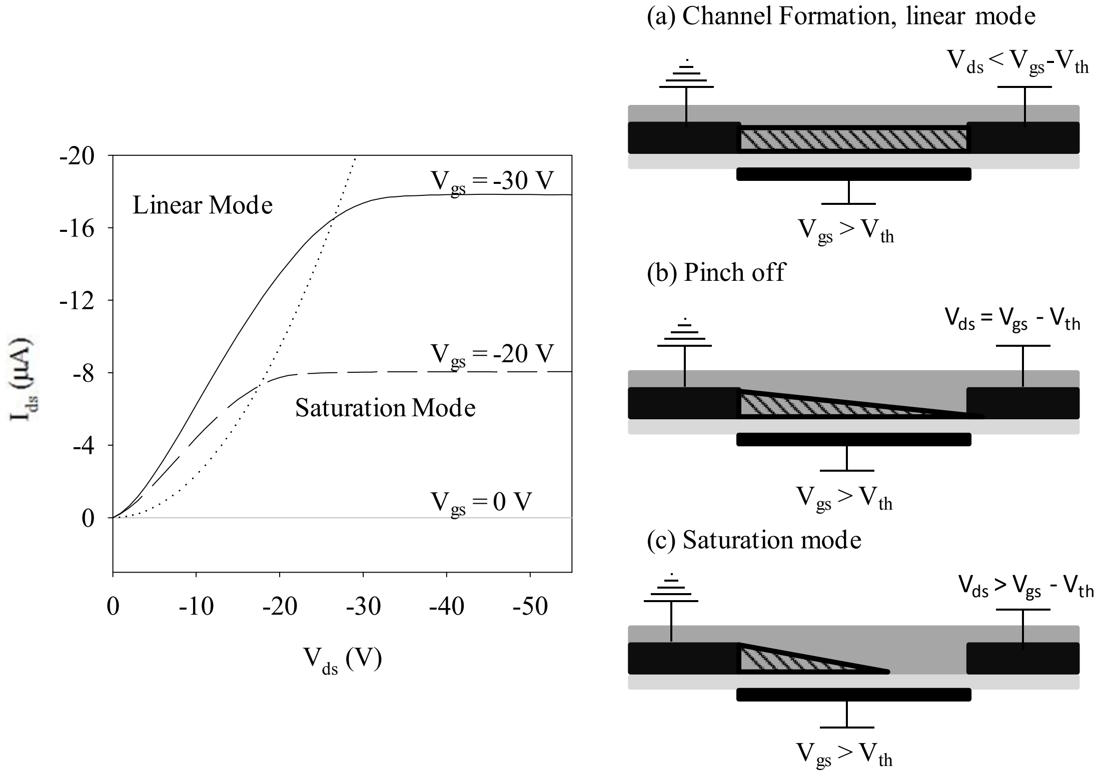

Figure 1.3 Graph of a rubrene thin film transistor current-voltage characteristic showing linear and saturation modes separated by dotted line, $V_{th} = 0.7$ V, $\mu_{sat} = 2$ cm^2/Vs. Diagrams (a) through (c) represent the conduction channel as a striped area for different operation modes.

1.3.1 The Organic Field Effect Transistor (OFET)

There has been debate over whether OSCs can be described using inorganic FET equations due to the OSC charge transport mechanisms, problems defining the threshold voltage due to the absence of a true inversion layer, and the gate voltage dependence of the mobility in many samples[1,16-18]. Some studies show that gate voltage dependence of mobility is caused by charge trapping sites at crystal boundaries, impurities, etc. [14] or that mobility varies with charge concentration [16,18]. Despite these issues, single crystal studies show that Equations 1.1 and 1.2 are generally satisfactory descriptions of OFET behavior [19,20].

Like inorganic semiconductors, organic semiconductors are typically undoped when used in thin film transistors. The OFET conduction channel is formed when charge flows in from electrical contacts in response to an applied gate voltage. The sign of the charge depends on the polarity of the gate voltage, and the concentration of charge is dependent on the matching of energy levels between the OSC, electrode contacts, and dielectric material [21]. Many small molecule OSCs, such as the materials used in this study (TIPS Pn and diF TES ADT), are hole carriers when paired with gold contacts due to matching of the highest occupied molecular orbital (HOMO) band in the OSC with the work function of the contact metal, see Figure 1.4, and are called “p-type” in analogy to doped inorganic semiconductors.

Diagram A.

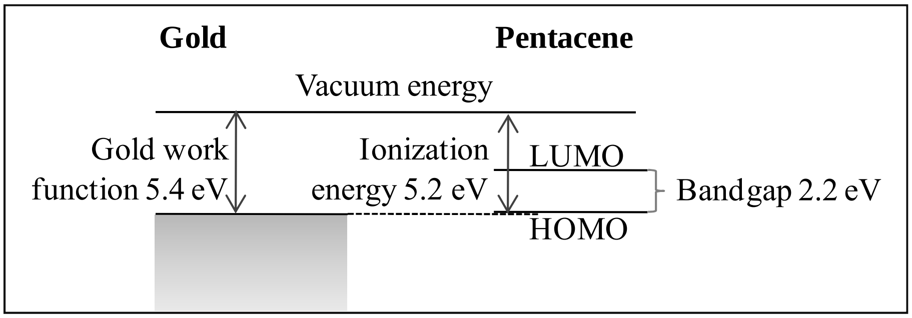

Diagram B.

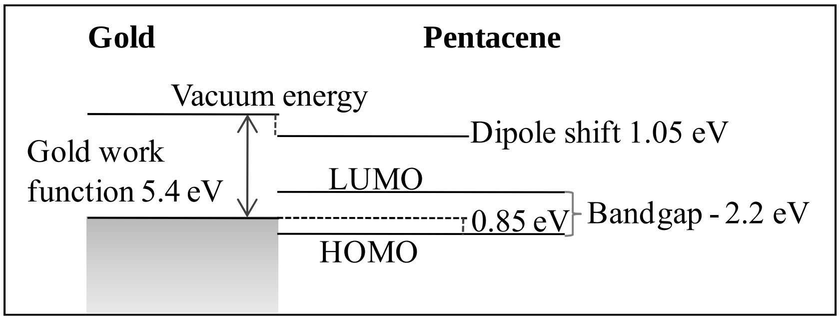

Figure 1.4 Energy diagrams of the gold/pentacene interface. Diagram A shows the vacuum energy levels, diagram B shows energy levels when the materials are in contact (shifted due to dipole energies at the interface) – from Reference [22], measured using photoelectron spectroscopy.

For many years commonly studied small molecule OSC materials, like pentacene and rubrene, showed higher hole conduction than electron not only due to the higher barrier for electron injection from the lowest unoccupied molecular orbital (LUMO) bands to commonly used high work function metals [23,24] but also due to larger HOMO bandwidths that favor hole conduction [25]. In addition, negative carriers are more likely than holes to be trapped by common chemical impurities that leach into the OSC in atmospheric conditions (i.e. oxygen and water), and by hydroxyl, silanol, or carbonyl groups common to many widely used dielectric materials [24-26]. Though these barriers hindered early work in n-type conduction, recent work has succeeded in synthesizing molecules with high electron mobility by lowering LUMO levels and increasing the air stability [2].

1.4 Transport in Organic Semiconductors

Transport in metals and inorganic semiconductors is described using a band model which is adequate to describe the electronic behavior of these materials [15]. However in organic semiconductors, which behave more like "semi-insulators," the electronic transport takes on a different form which is still being investigated.

Electronic transport in OSCs involves the delocalized states associated with the π-orbitals of conjugated molecules. Hole (or electron) conduction between molecules, bonded by weak Van der Waals forces, depends on the overlap of the HOMO (LUMO) band between neighboring molecules. Charge modulated infrared measurements on polymer OSCs show evidence of strongly bound polaron carriers (charge with accompanying lattice distortion) [7]. However, on highly ordered small molecule rubrene the possibility of band-like transport of light quasiparticles up to room temperature is observed [27], and low temperature transport measurements hint the presence of band-like conduction [24]. Band-like transport in current-voltage measurements has been observed in polycrystalline TIPS Pn when charges in shallow traps are released using moderate V_{ds} at low temperature, though this is not true extended state conduction but delocalization over only a few molecules [28]. In some studies it has been shown that one device can show multiple transport "regimes" depending on temperature and carrier concentration [18,29,28].

Charge transport has been modeled within the limiting cases of localized hopping between molecules and coherent, band-like transport in extended states. Developing a model of transport is a challenge that requires combining the competing evidence of each. Computational models have shown that the charge conduction is a strong function of crystal structure and packing [30], and that localization of charge can be a dynamic process in small molecule OSC due to the thermal motion of molecules in the lattice decreasing the charge transfer intergral (which is related to the overlap of energy levels in neighboring molecules) [31]. Since the thermal vibrations are large at high temperature and small at low temperature, the material with this type of "thermal" localization will show a band-like mobility increase with decreasing temperature.

In pentacene, TIPS Pn, and diF TES ADT (and others) the molecules pack in a layered structure: Figure 1.5 shows the packing of a TIPS Pn layer in a single crystal and Figure 1.6 shows polarized FTIR spectra of a typical thin film crystal grown out of solution in our lab. In these materials conduction takes place in the plane of the a and b axis (in the plane of the crystal) with very little electrical transport along the c-axis (between layers) [29,32]. Charge transport anisotropy in the a-b plane of TIPS Pn is between 3.5-10, and the highest conductivity is near the a-axis [32-34]. In situ studies of charge conduction in pentacene during thin film formation show that most of the charge is carried on the 2-7 monolayers nearest to the gate dielectric [35].

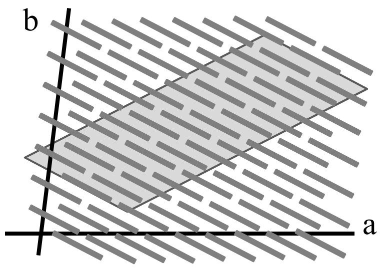

Figure 1.5 a-b plane stacking of TIPS Pn,the pentacene backbone is represented by short grey lines. Large grey shaded area shows the approximate orientation of a single crystal with respect to the a-b plane. Adapted from Reference [33].

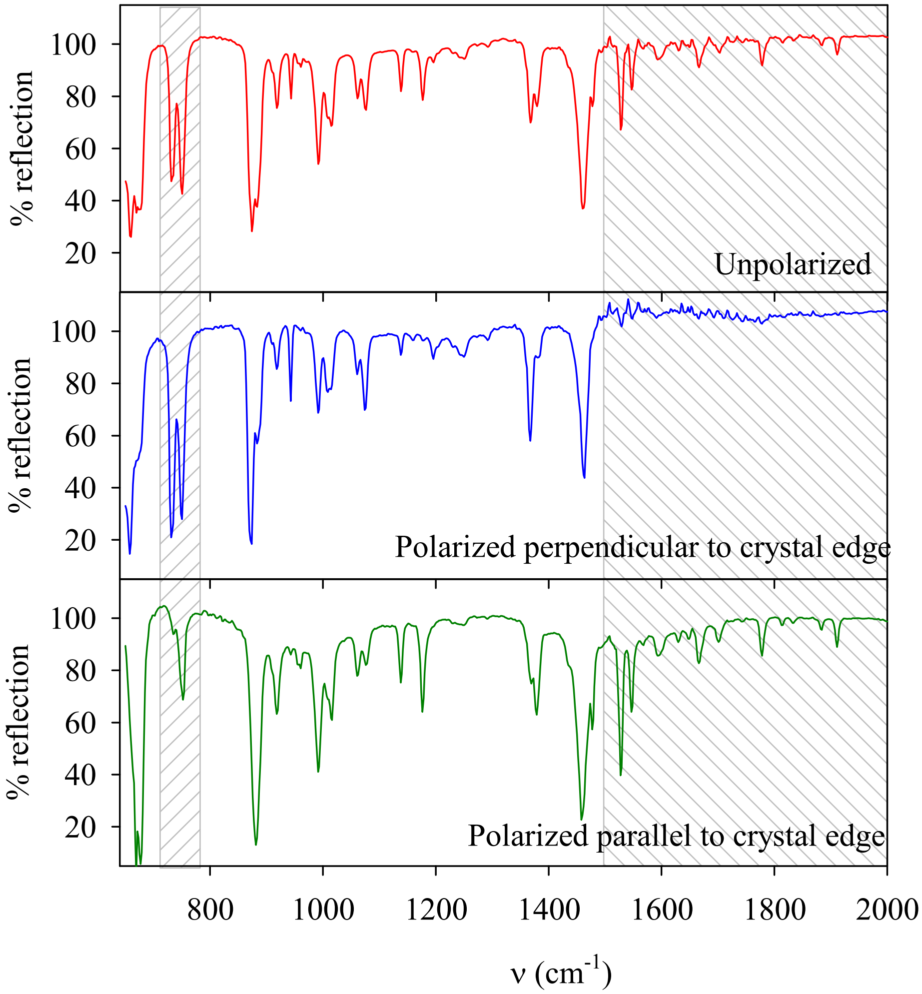

Figure 1.6 Unpolarized and polarized (with wire grid polarizer) infrared spectra of a thin film TIPS Pn crystal grown out of solution on gold. Shaded areas show areas where the spectrum is most strongly polarization dependent, showing alignment of molecules.

1.5 Measuring slow charge using voltage modulated infrared transmission

Previous studies using modulated infrared reflectance and transmittance in our lab focused on measuring the slow moving charge carriers associated with charge density waves in one-dimensional conductors such as $K_{0.3}MoO_3$ (potassium molybdenum oxide, also called blue bronze.) Success in this measurement inspired a study of slow charge transport in organic semiconductors.

1.5.1 Charge Density Waves

In one dimensional metals at low temperatures, electron-phonon interactions give rise to a state characterized by a periodic lattice distortion and a periodic modulation of the electronic charge density called a Charge Density Wave (CDW) [36]. CDWs are pinned in place in the material by defects such as impurities, but can be depinned by applying a voltage $V > V_{on}$, the onset of polarization. During polarization, the CDW is depinned within the crystal, bunching on one end and rarifying on the other end. At V_T ($> V_{on}$) the CDW is depinned at the contacts and charge is transported by the CDW, which results in an oscillating component to the current [37,38]. This effect is observed in certain quasi-one-dimensional materials, such as blue bronze [39].

The variation of phase in the charge density under polarization is screened by free carriers [37,40] which results in a change in the infrared transmission, as observed by Itkis and Brill [41]. Distortion of the CDW under applied voltage increases transmission on the positive side of the sample and decreases it on the negative side over a wide infrared spectral range, and this change is proportional to the local CDW strain. Measuring the changes in IR transmission allows one to determine the position and time dependent changes in the collective mode of CDW phase [38, 40-42].

At the beginning of my time in the lab, we studied the behavior of polarization onset in blue bronze using the electro-optic response [42]. This study aimed to measure critical changes in the CDW phase dynamics within 10% of the onset voltage for CDW polarization (in the elastic and diffusive limit), where the diffusion constant (D) is expected to diverge. Near threshold, the response time τ is inversely proportional to D, which was measured using the square wave frequency and voltage dependent electro-optic response for voltages within 6-10% of the onset voltage. Critical behavior (decrease of τ with voltage) was not observed down to $1.06V_{on}$, setting $|V/V_{on} - 1| < 0.06$ as the upper limit of the critical region.

1.5.2 Light measurements of OFETs

Based on the success of electro-optic measurements in detecting polarization in CDW materials, we began a project to look at organic semiconductors using a similar technique. In addition, voltage modulated IR and visible light measurements have been used to study the charging and conduction mechanisms in organic transistors: measurements of the optical properties have yielded the spatial dependence of the charge within a transistor [8,16], changes in far infrared absorption with applied voltage [6], changes in molecular vibration frequencies (including the creation of broad-band polarons) [7,16], and properties of the HOMO and LUMO bands [43].

The materials used in this study are single crystal, small molecule OSC thin film transistors. When voltage is applied to the gate, charges accumulate on the surface of the semiconductor closest to the gate dielectric. This charge originates at the contacts, and is not present when $V_{gs} = 0$. Fisher et al. observed broad-band energy absorption in the mid to far infrared using charge modulation spectroscopy on rubrene single crystal transistors with a spectrum suggestive of a Drude response [6]. Similarly, in our measurements transistors show a broadband absorption in the mid-infrared (425-1100cm^{-1}) when infrared light is reflected off the gate, as shown in Figure 1.7.

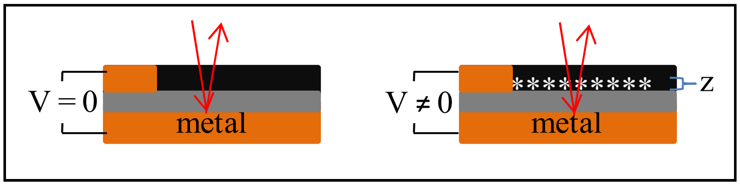

Figure 1.7 Simplified picture of light passing through a charged layer induced by a voltage applied to a metal beneath a dielectric barrier.

In a simplified view, assuming the charges are free to interact with incoming light and move along the interface, the change in reflection due to absorption by charges on a two-dimensional layer of charge can be estimated to the first order:

$$\frac{\Delta R}{R} = \frac{I_0 e^{-\alpha x} - I_0}{I_0} \qquad \text{Equation 1.3}$$

where x is the thickness of the charged area, I_0 is the intensity of light without voltage applied, and a is the extinction coefficient. Expanding for small αx:

$$\frac{\Delta R}{R} \approx 1 - \alpha x + \frac{\alpha^2 x^2}{2!} + \cdots - 1 \approx -\alpha x \qquad \text{Equation 1.4}$$

In measurements of a transistor with a metallic gate the reflected light will pass through the active layer twice, therefore x = 2z where z is the thickness of the conducting layer. Using the low conductivity (i.e. large scattering) limit of the extinction coefficient [44]:

$$\alpha \approx \frac{\rho \mu_{lin}}{\varepsilon_0 c} \qquad \text{Equation 1.5}$$

we then have:

$$\frac{\Delta R}{R} \approx -\alpha x = -2z \frac{\frac{\rho_{2D}}{z} \mu_{lin}}{\varepsilon_0 c} = -2\alpha_{2D} \qquad \text{Equation 1.6}$$

for absorption through a conducting layer of thickness z.

1.6 Charge Flow in a 1D channel

To facilitate an understanding of dynamic (AC) characteristics of OFETs, we have used a simple model to calculate the dynamics of charging and discharging of a transistor. Charge flow in an OFET has been studied with focus on their steady state (DC) properties to compare with current-voltage measurements [45], and the dynamic current response is addressed in some studies for samples with high contact resistance [46]. Below is a solution to the model for charge conduction in transistors with no contact resistance, solving for position and frequency dependence of the charge.

For our model, we assume a constant width for the semiconductor between the drain and source electrodes with length L, that all the charge is at the interface with the dielectric [35], and that there is negligible leakage through the gate dielectric [16]. We neglect fringing fields so that the problem is one-dimensional and the voltage at a position x is proportional to the charge density: V(x,t) = ρ(x,t)/C, where C is the capacitance to the gate and ρ is the charge per unit area. Assuming the current density between the drain and source electrodes is limited by diffusion and conductance in the OSC:

$$j = -D\frac{\partial \rho}{\partial x} - \mu\rho\frac{\partial V}{\partial x} = -(D + \frac{\mu\rho}{C})\frac{\partial \rho}{\partial x} \qquad \text{Equation 1.7}$$

$$\frac{\partial \rho}{\partial t} = -\frac{\partial j}{\partial x} = \left(D + \frac{\mu \rho}{C}\right)\frac{\partial^2 \rho}{\partial x^2} + \frac{\mu}{C}\left(\frac{\partial \rho}{\partial x}\right)^2 \qquad \text{Equation 1.8}$$

where D is the diffusion constant and μ is mobility, which we take as a constant as expected for a single crystal semiconductor with low defects. The case of a charge dependent mobility is discussed in Chapter 4.

To simplify calculations and measurements, we focus on the situation where $V_{ds} = 0$ and the only current is that which is induced by the changing gate voltage. For square wave voltages switching between 0 and ρ_0/C applied to the gate,

$$\frac{\partial \rho}{\partial t} = \left(D + \frac{\mu \rho_0}{2C}\right)\frac{\partial^2 \rho}{\partial x^2} + \frac{\mu}{C}\left[\left(\rho - \frac{\rho_0}{2}\right)\frac{\partial^2 \rho}{\partial x^2} + \left(\frac{\partial \rho}{\partial x}\right)^2\right] \qquad \text{Equation 1.9}$$

As boundary conditions, we assume that there are negligible contact impedances and injection barriers, so that at the source and drain, $\rho(0,t) = C\,V_{gs}(t)$ and $\rho(L,t) = C\,V_{gd}(t)$. This can be solved numerically for different frequencies and values of $D/\mu V_{gs}$. The Einstein relation for the diffusion constant, $D \sim \mu k_B T/e$, so that $D/\mu \approx 26$ mV at room temperature, which could be slightly enhanced by a factor of 1.2 – 1.8 [47]. The diffusion constant is then negligible ($D/\mu \ll V_{gs}$) when the applied gate voltage $V_{gs} > 1$ V; therefore only solutions for $D \approx 0$ are presented here.

Figure 1.8 shows the time dependence of ρ (x= L/2, L/3, L/6) at a few square wave frequencies defined as a multiple of the characteristic frequency $F_0 = \mu V_{gs}/(2L^2)$. One striking aspect of the response in the channel is the asymmetry of charging and discharging. When charging, the charge density adjacent to the source and drain, and therefore the conductivity, is at its maximum value, but when discharging, the charge density and conductivity at the contacts is zero, creating a bottleneck for charge to leave the interior of the channel. (This bottleneck effect is not significantly changed by including a small but finite D, e.g. $D = 0.02\mu V_{gs}$, shown in Figure 1.9.) This asymmetry was noticed and discussed by Matsui and Hasegawa [5]. A consequence is that the average charge becomes greater than $\rho_0/2$ (the average expected for a linear response.)

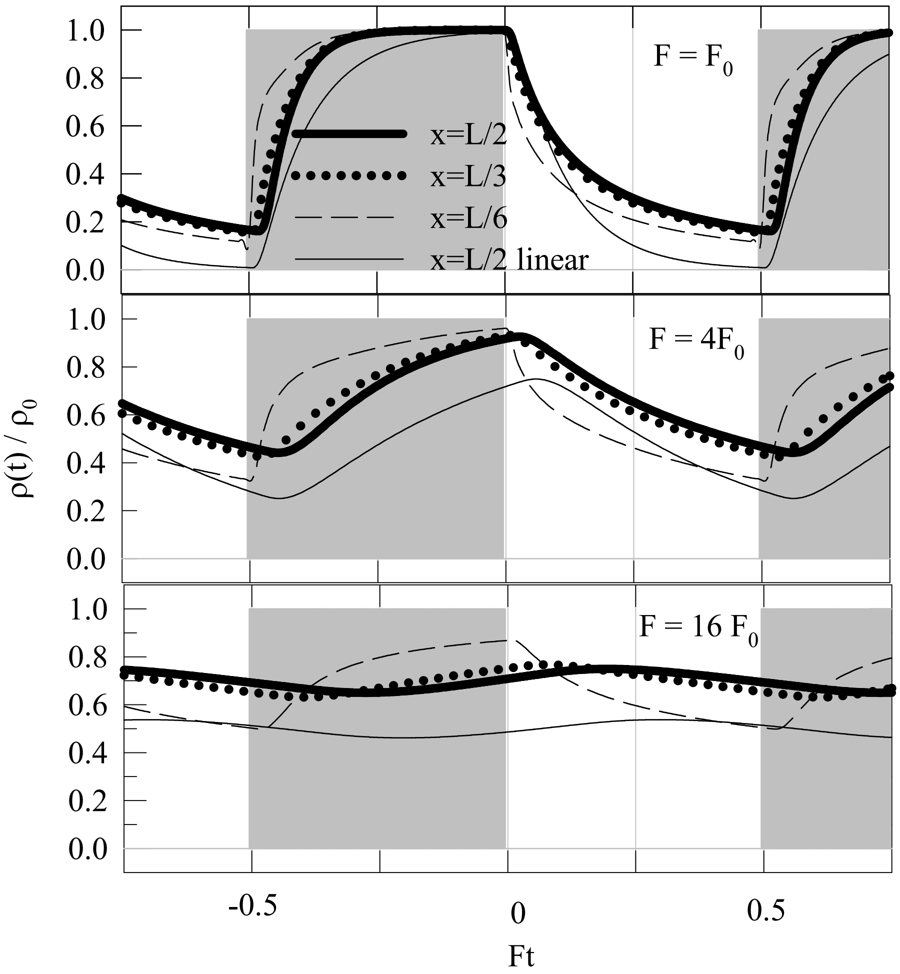

Figure 1.8 Plots of solution to Equation 1.9 for varying frequencies of applied gate voltage and at three positions within the transistor, with $V_{ds} = 0$. Also shown is the linear response, which does not include the terms in brackets in Equation 1.9. The square wave applied voltage is diagrammed as a gray background when voltage is "on" ($q = C/V_{gs}$) and no color for "off."

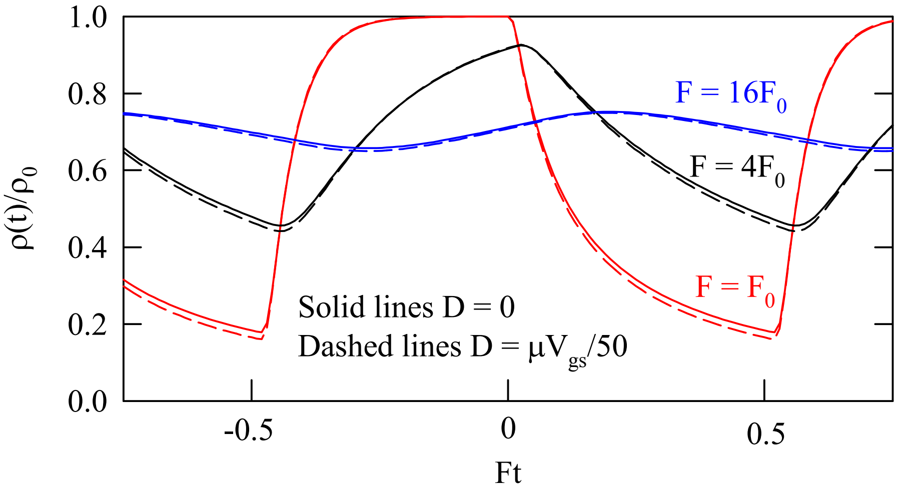

Figure 1.9 Solutions to Equation 1.9 comparing D = 0 to D = $0.02\mu V_{gs}$.

Comparing the response at different positions within the sample shows that the response at L/6 (closest to the contact) is significantly different from the response at L/2 and L/3, where the response is very similar, especially at low frequency. The similar response is due to the charge flowing from contacts on either end of the sample. This result becomes important in measurements, where the measurement area is finite and the measurement area may not be precisely in the center of the channel.

The first Fourier component of the charge density at various gate voltage frequencies is shown in Figure 1.10. The L/2 and L/3 positions have similar responses, and are qualitatively similar to over-damped harmonic oscillators; in particular at high frequency the in-phase response becomes inverted at F ~ 4 F_0 where charge is still flowing into (out of) the center when the voltage is turned off (on). In contrast, at L/6 the in-phase response has a long tail (positive signal) extending to high frequencies reflecting the rapid diffusion of charge from the nearby contact.

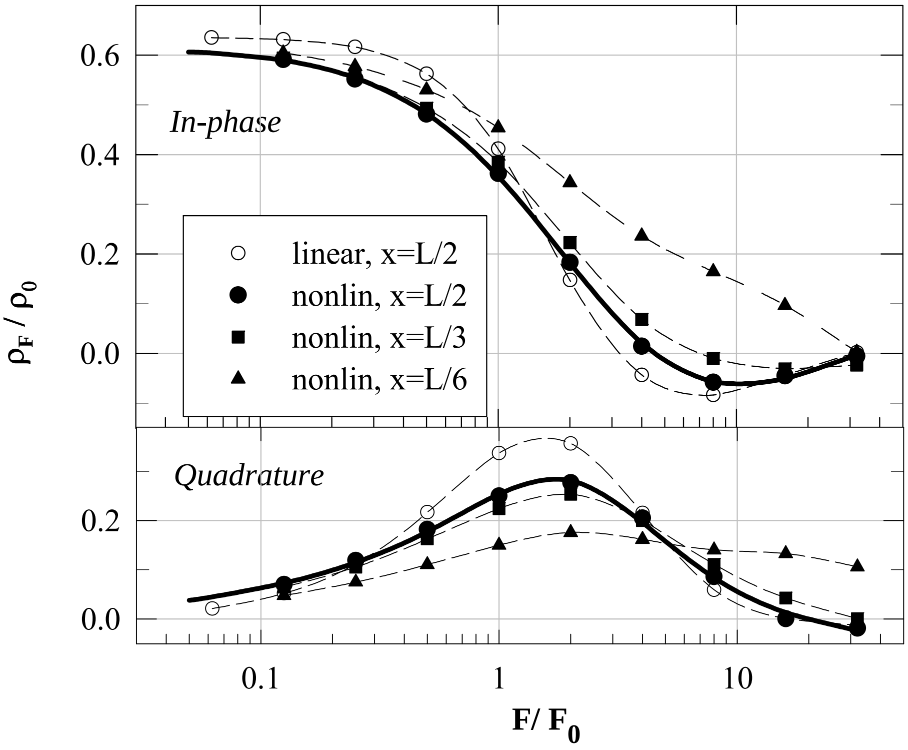

Figure 1.10 Fundamental fourier component of the solution to Equation 1.7 at three distances from the drain contact, also included is the solution to the linear equation at the center of the channel. The solution to the nonlinear equation at the center is fit to a rational expression which is used to fit electro-optic data (Equation 4.1.) For other cases, the curves are guides to the eye.

CHAPTER 2 **Experiment: Equipment and Sample Preparation**

This section reviews the electro-optic system, spectrometers, and sample preparation.

2.1 **Experimental set up**

The original purpose of the electro-optics system in our laboratory was to study charge density wave materials, from 1994 to 2008. Since 2008 we have added a Fourier transform infrared spectrometer (FTIR) for quicker measurements of the infrared reflection and transmission spectra. The outline of the present system is shown in Figure 2.1 and a detailed diagram of the optical bench is shown in Figure 2.2. The main system components are the lasers, optical table, microscope, and FTIR.

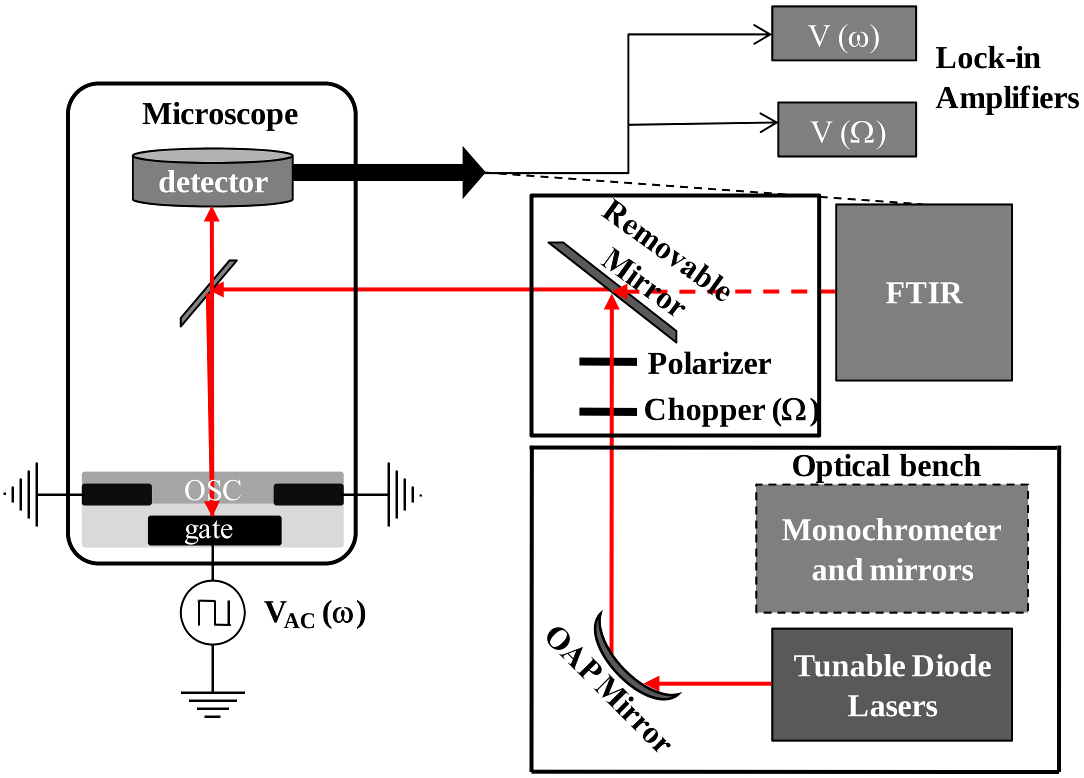

Figure 2.1 Diagram of the optical set up for infrared measurements at the University of Kentucky.

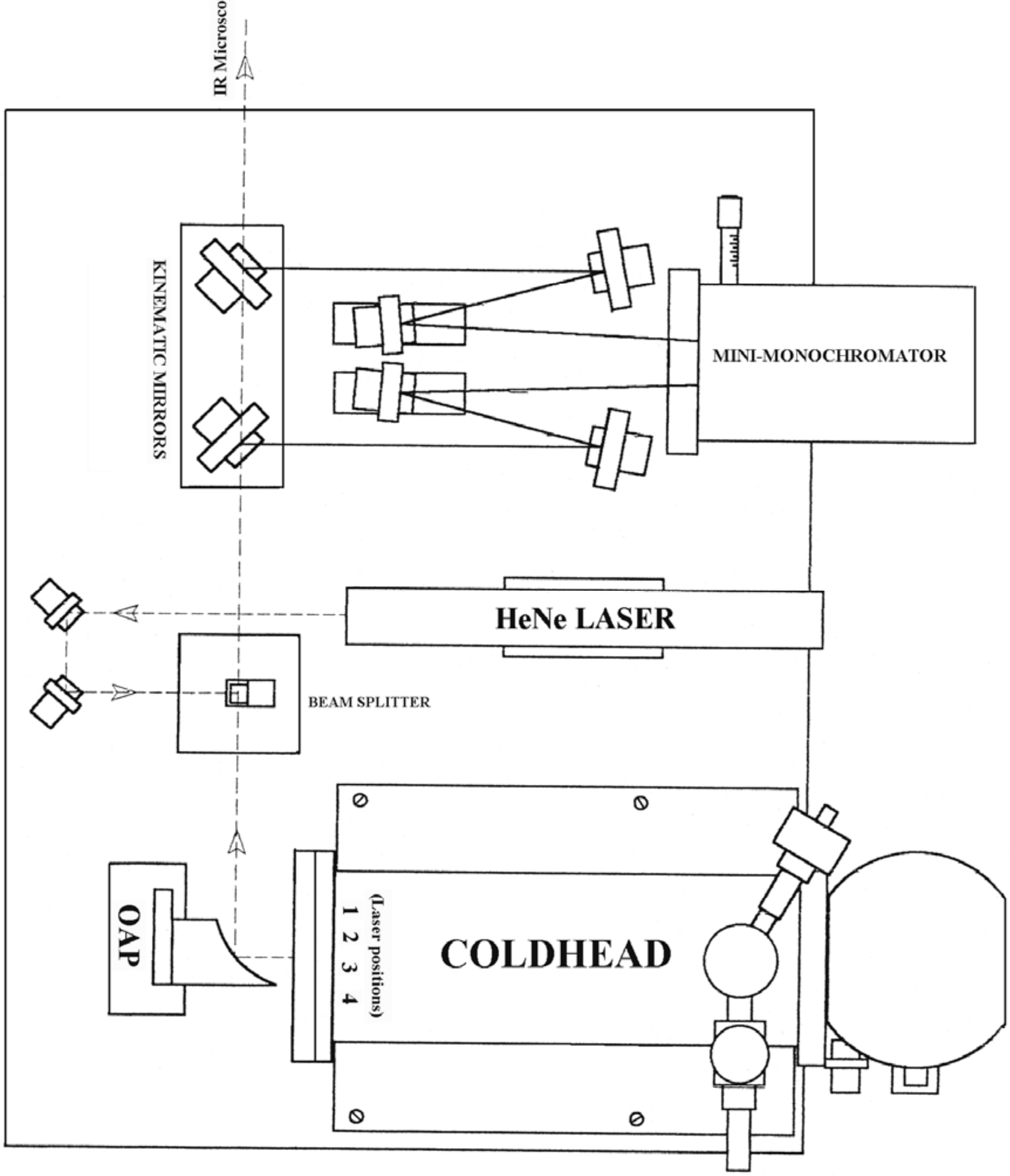

Figure 2.2 Optical bench with detail. The kinematic mirrors are in place only during laser calibration, and the beamsplitter is only used when the HeNe alignment laser is in use. Diagram from Ram Rai's thesis [48].

2.1.1 Lasers

Infrared tunable diode lasers are used in the lab and are composed of $Pb_{1-x}Sn_xSe$ (lead-tin-telluride) from Laser Components, Inc. The four original tunable diode lasers used for electro-optics measurements were installed in 1997 to replace a broadband globar source. Tunable diode lasers can be varied semi continuously over portions of the infrared spectrum (depending on alloy composition, temperature and applied current) which makes them well suited for our wavelength dependent electro-optic studies. The composition (x-value) can be controlled during crystal growth and is used to vary the bandgap of the material. Lasing wavelength depends on bandgap (E_g) as:

$$\lambda = \frac{hc}{E_g} \qquad \text{Equation 2.1}$$

where h is Planck's constant, and c is the speed of light. The precise modal output can be further controlled by the refractive index and cavity length:

$$\lambda_m = \frac{2nl}{m} \qquad \text{Equation 2.2}$$

where n is the refractive index, l is the length of the cavity, and m is the number of half wavelengths in the cavity. The bandgap and refractive index are temperature dependent [49], therefore the lasing wavelength can be controlled by varying the temperature.

The four lasers are mounted on the cold finger of a closed cycle refrigeration system (CTI 8200 compressor) in which high pressure helium gas is pumped through the system and cools upon expansion. This keeps the base temperature between 13 – 19 K. The heat and current is controlled using a microprocessor controlled system (Laser Components Inc, L5830). The four lasers used for electro-optic measurements have a collective range of 425cm^{-1} (23.5μm) to 1150cm^{-1} (8.7μm.) The wavenumber range for each laser along with temperature range and current applied are given in Table 2.1.

Table 2.1 Laser wavelengths and operating conditions.

Laser	Temperature Range (K)	Current (mA)	Wavenumbers (cm^{-1})
1	20-80	550	425-625
2	20-40	600 (900)	620-680 (650-720)
3	20-90	750	700-1000
4	20-75	400	975-1150

Due to temperature cycling and age, the lasers need to be recalibrated periodically. This is done using a monochromator located in the optical table, Figure 2.2. At each temperature and current setting, the laser will have between 1 and 10 modes. Mode wavelength and intensity is measured for temperatures about 2 K apart using the monochromator and lock-in amplifier, tuned to the frequency of the chopper. The monochromator position is weighted by the signal intensity of each mode, and this weighted average is used to calculate the average wavelength at a laser temperature. An example calibration curve is shown in Figure 2.3, the error bars signify the broadening of the lasing wavelength through multiple modes. The calibration data is fit to a polynomial equation that is used to calculate the average wavelength from operating temperature. For electro-optic measurements all the laser modes at one temperature are collected.

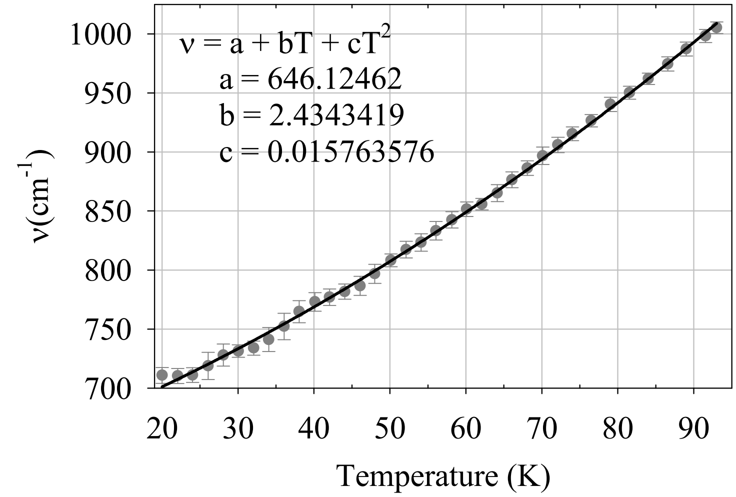

Figure 2.3 Example calibration data for a laser. Solid line shows a fit to the data.

The main source of noise in measurements using the lasers is the mechanical vibration and motion of the lasers due to the closed cycle refrigeration system. In principle, the lasers could be cooled with liquid nitrogen or helium dewars, but the cost of keeping the lasers cold for long periods made such measurements tedious, and repeated cooling can destroy the lasers by causing their contact resistance to increase. We experimented with using thermal sources with parabolic mirrors (in place of the lasers) which have much less noise (and do not require cooling), but the signal was small so that the signal/noise was less than with the lasers.

2.1.2 Optical Table

The optical table houses mirrors, the monochromator for calibrating the lasers, and an alignment laser, shown in Figure 2.2. An off-axis parabolic (OAP) mirror is used to collimate the laser light, and for electro-optic measurements the kinematic mirrors diverting the laser light through the monochromator are removed, so all the light (i.e. all the modes) are collected. The beamsplitter can be removed and is in place only during alignment using the HeNe laser. A removable mirror is used to switch between laser and FTIR measurements using the microscope, and a chopping wheel, used to facilitate lock-in measurements, is placed between the optical table and the infrared microscope.

2.1.3 Microscope

The Thermo Continuμm infrared microscope is used to reflect or transmit light on the sample, using a measurement area between 10μm × 10μm and 200μm × 200μm. The microscope can be used in either reflection or transmission mode, but for this study was only used in reflection mode due to the configuration of the field effect transistors.

Two mercury cadmium telluride (MCT) detectors are mounted in the microscope for infrared measurements using either the FTIR or lasers. Both MCT detectors operate at 77 K, and are cooled using liquid nitrogen which can be stored for over 8 hours in the separate dewars that house the detectors. The first detector covers the spectral range from 400 cm^{-1} – 1300 cm^{-1} with peak detectivity at 465cm^{-1}, and the second detector covers 600cm^{-1} – 4000 cm^{-1} with peak detectivity at 740 cm^{-1} and has better signal-to-noise. The second detector was used most frequently, while the first detector was only used for measurements in the low wavenumber range (< 600 cm^{-1}.)

2.1.4 Spectrometers

FTIR at the University of Kentucky

The spectrometer used in the lab is the Thermo Scientific Nicolet 6700. The compatible design of the FTIR and microscope makes it possible to use the microscope sample stage and detectors, instead of the FTIR internal detector and sample space, to measure spectra in the same configuration as electro-optic measurements. Example spectra of TIPS Pn thin film and bulk spectrum are shown in Figure 2.4. To switch the input of the microscope between the lasers and FTIR light source, the light from the FTIR source is sent out to the microscope through a port hole (KRS-5 window) on the side of the spectrometer. The light is then reflected off the sample and into the microscope detector, and the resulting interferogram is Fourier transformed by OMNIC software that came with the FTIR. The OMNIC software also allows for normalization to the background and other spectral manipulations. Background normalization was the only feature used regularly, and most background spectra were reflection off of a standard gold slide (R = Signal with sample/ Signal with gold). An example background single scan of reflection off a gold slide is shown in Figure 2.5.

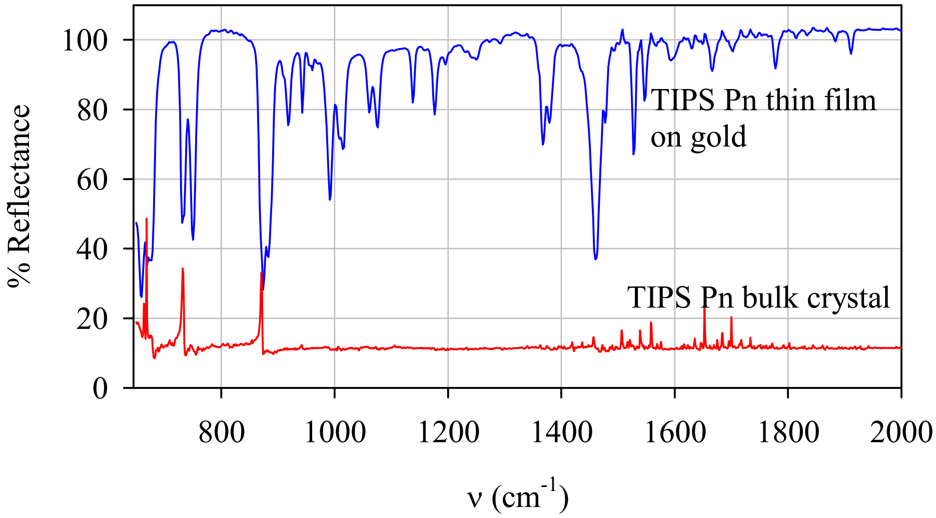

Figure 2.4 TIPS Pn spectra taken with FTIR and microscope, taken in reflection mode. The bulk crystal spectrum is reflection off of a smooth surface, and the thin film spectrum was taken for a crystal grown on gold (and is therefore dominated by the absorption through TIPS Pn.)

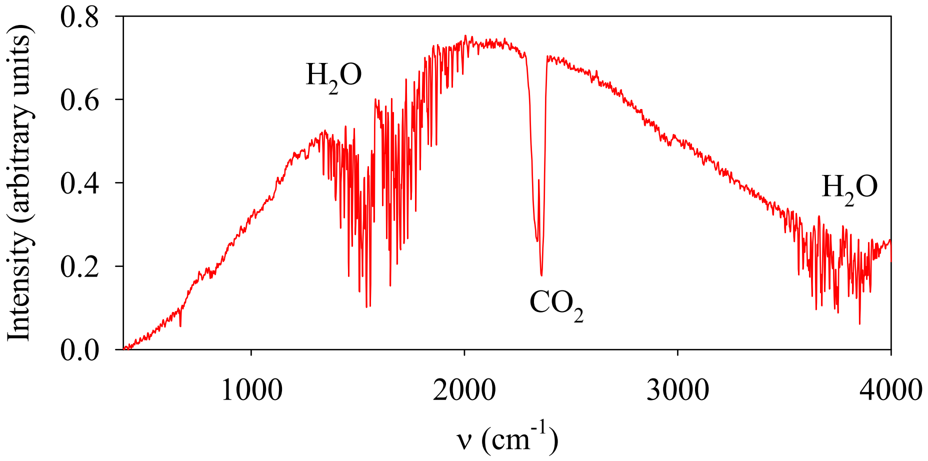

Figure 2.5 Single scan spectrum of reflection off a gold film, the overall shape shows the blackbody curve from the FTIR light source interrupted by absorption through air, notably water and carbon dioxide [50].

FTIR at the National Institute of Standards and Technology

Measurements taken at the National Institute of Standards and Technology (NIST) used the Nicolet 8700 Research FT-IR Spectrometer, which is very similar to the Nicolet 6700 with the addition of several features which were not used in this study. The sample was mounted on a reflection accessory – which could reflect the light off the sample at angles between 30° to 70° – in the sample compartment of the FTIR. The sample compartment was nitrogen purged for one hour before starting measurements to limit OSC degradation and background lines in the FTIR spectrum. To study changes in phonon frequencies with molecule charging, voltage dependent spectra were taken by collecting single scan spectra with $V_{gs} = 0$ for approximately 50 scans ("off"), then collecting with $V_{gs} \neq 0$ ("on") for 50 scans (scans are averaged to produce a single line spectrum by the OMNIC software.) This process, automated using LabView, was repeated approximately 50 times to obtain a high signal to noise ratio of the change in spectra caused by the applied voltage, and each scan was kept relatively short to reduce drift. Data analysis was performed using Mathematica and SigmaPlot. A program was written which added all "on" and "off" spectra into two files and used these files to compare the data. Typically the differences were compared by taking the ratio (on/off) or the normalized difference ((on-off)/off.) Spectra collected at NIST are presented in Chapter 3.

This same measurement was attempted using the microscope and FTIR at the University of Kentucky, but due to the light limiting optics in the microscope the signal-to-noise was too low to observe expected voltage dependent changes in spectra. The random noise after ~ 10 hours of signal averaging was slightly above the signal level ($\Delta R/R \sim 10^{-4}$, see Figure 3.6) and was affected by long term drift in the microscope.

Raman Spectrometer

Raman measurements were taken in Dr. Beth Guiton's lab at the University of Kentucky using the HORIBA Jobin Yvon LabRAM HR system. The sample is mounted on an optical microscope with three objectives, 10x, 50x and 100x; the resolution of the microscope at 100x is 2 μm × 2 μm. The Raman spectrometer light source is a 5 mW HeNe laser. In order to avoid burning holes in the OSC sample, intensity is adjusted using a continuous variable filter to ~ 0.15 mW. The signal is reflected off the sample, detected by a CCD array, and processed by LabSpec 5 software. An example Raman spectrum of a bulk TIPS Pn crystal is shown in Figure 2.6, spectra of a thin film using FTIR and Raman spectroscopy are shown in Figure 2.7.

Voltage modulated Raman spectra, with which we again hoped to study phonon changes with molecule charging, were attempted using a similar method to that described for the FTIR at NIST above; unfortunately these measurements could not achieve a high enough signal-to-noise due to the digitizing CCD detectors.

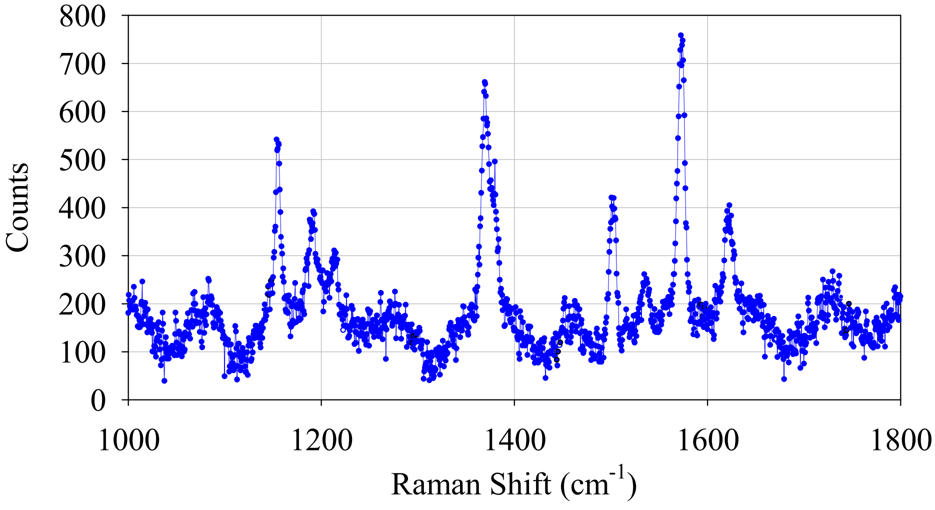

Figure 2.6 Raman spectrum of a bulk TIPS Pn crystal, background subtracted.

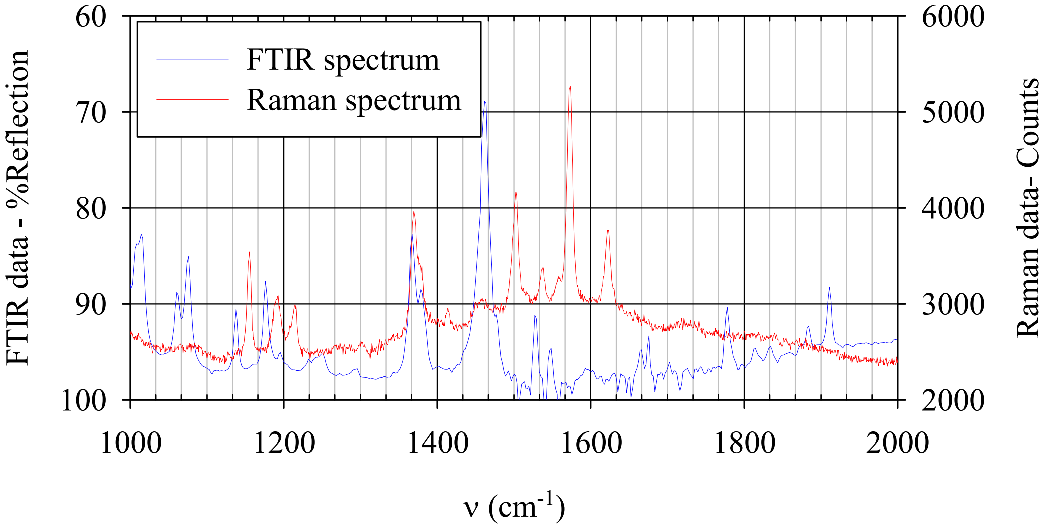

Figure 2.7 FTIR and Raman spectra of TIPS Pn thin film on gold.

2.2 Electro-optic measurements using the infrared lasers

For the best signal-to-noise measurements of voltage modulated reflection, relative changes in reflectance are measured using the lasers with the sample mounted in the microscope and are normalized to a simultaneous measurement of the total reflectance. A unipolar square wave voltage $F = \omega/2\pi$ is applied to the sample gate, using the HP 33120A frequency generator and a home built 10x amplifier, and the infrared beam is chopped at $\Omega \approx 370$Hz. The modulated signal reflected off the sample is detected using one of the two MCT detectors mounted in the microscope, and the output is sent to two lock-in amplifiers connected in parallel, as shown in Figure 2.1. The lock-in amplifiers, Princeton Applied Research 5302 and Stanford Research Systems SR830 DSP, are referenced to the chopping frequency and function generator frequency; the ratio of these two signals gives the value of $\Delta R/R$. Changes in reflectance are measured as $\Delta R = R(V) - R(0)$ so that a positive value of ΔR signifies an increased reflection, while negative signifies a decreased reflection (by absorption in the semiconductor.) The signal is measured in-phase and in quadrature (90° out of phase) with the applied square wave voltage.

The frequency dependence of the gain and phase shift of the microscope detector and lock-in amplifier were measured with a chopped light signal in order to calibrate the system. The maximum speed of our high frequency chopper used to perform the calibration limited our measurements to frequencies below 20 kHz, and low frequency (less than ~ 100 Hz) measurements were limited by the noise of the detector and lasers. Measurements were also normalized to the frequency dependence of the gain and phase shift of the amplifier and function generator.

The Stanford SR830 lock-in, function generator, and Hewlett-Packard multimeters (used to measure the signal from the Princeton 5402 lock-in) were interfaced with the computer through a GPIB (general purpose interface bus) board for measurements early in the study; later the interface was changed to a GPIB to USB (universal serial bus) interface compatible with a new computer. Programs to collect data were written in QuickBasic: one program is used to measure spatial, wavelength, and voltage dependent data in which the user makes changes to the sample and uses the program to measure and organize the data; frequency dependence of the signal is measured using an entirely automated program where the function generator frequency is set by the program.

2.3 Current-voltage measurements

Current-voltage (IV) characteristics are taken for each transistor studied to assess the quality and operating characteristics. For measurements at the University of Kentucky, we use the circuit diagrammed in Figure 2.8. Voltage is applied to the gate and drain using two grounded DC sources. The drain current (I_{ds}) is obtained by measuring the voltage across a 1 MΩ resistor (connected in series with the drain contact) using a multimeter with floating ground, and precise values of the drain to source voltage are measured using a Hewlett Packard multimeter grounded through 10GΩ. Example IV data are shown in Figure 2.9 for a TIPS Pn sample on polymer dielectric (TIPS/PVP Sample 3.) Using the current-voltage data, the average mobility can be calculated using standard equations for linear and saturation regions, discussed in Section 1.3. For TIPS/PVP Sample 3 the linear mobility is $\mu_{lin} = 0.12\ cm^2/Vs$ (L = 250 μm, W = 375 μm and d = 500 nm.)

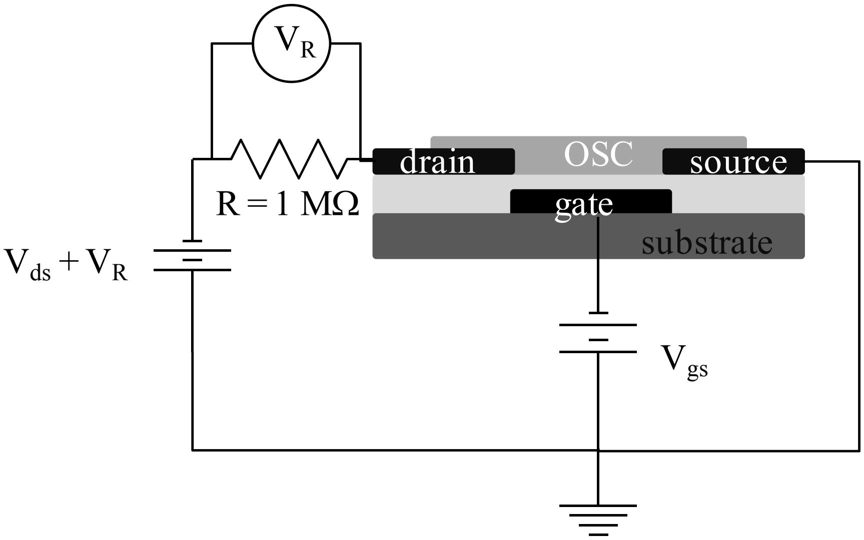

Figure 2.8 Circuit diagram for current-voltage measurements of FET.

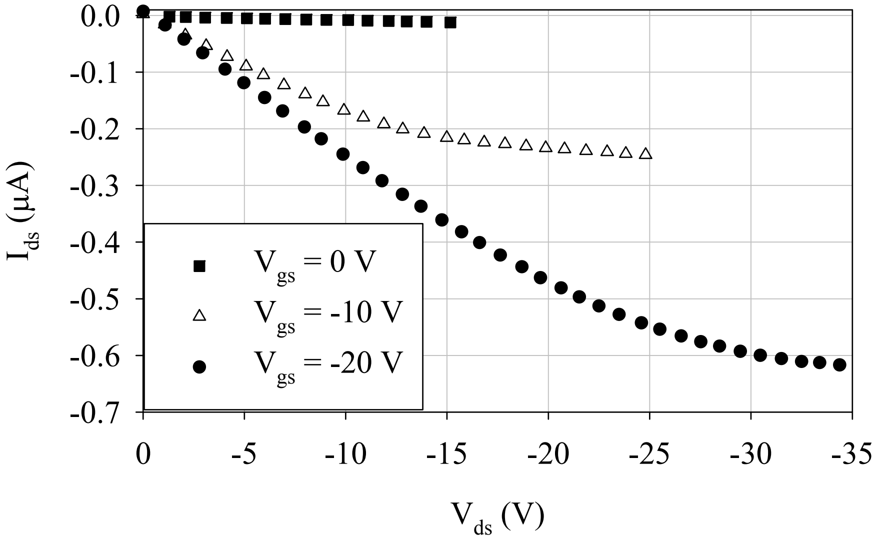

Figure 2.9 Current-voltage characterization of a TIPS Pn transistor with polymer dielectric measured at the University of Kentucky (TIPS/PVP Sample 3.)

In current-voltage characterization of organic transistors it is often the case that the drain to source current decreases over time and mobility values can change an order of magnitude in a few minutes under applied voltage; these effects are often attributed to gate bias stress [4,51]. We observed a similar effect in our IV measurements, and adopted the strategy of taking measurements after 15 seconds at the set V_{ds}, and allowing 60 seconds between changes in the gate voltage.

Current-voltage data taken at National Institute of Standards and Technology (NIST) were measured using a probe station and semiconductor parameter analyzer. Data collection was automated using LabView and had preset measurement times. Example data of a spin cast diF TES ADT transistor are shown in Figure 2.10, $\mu_{lin} = 0.03$ cm^2/Vs, channel length L = 50 μm and channel width W = 820 mm.

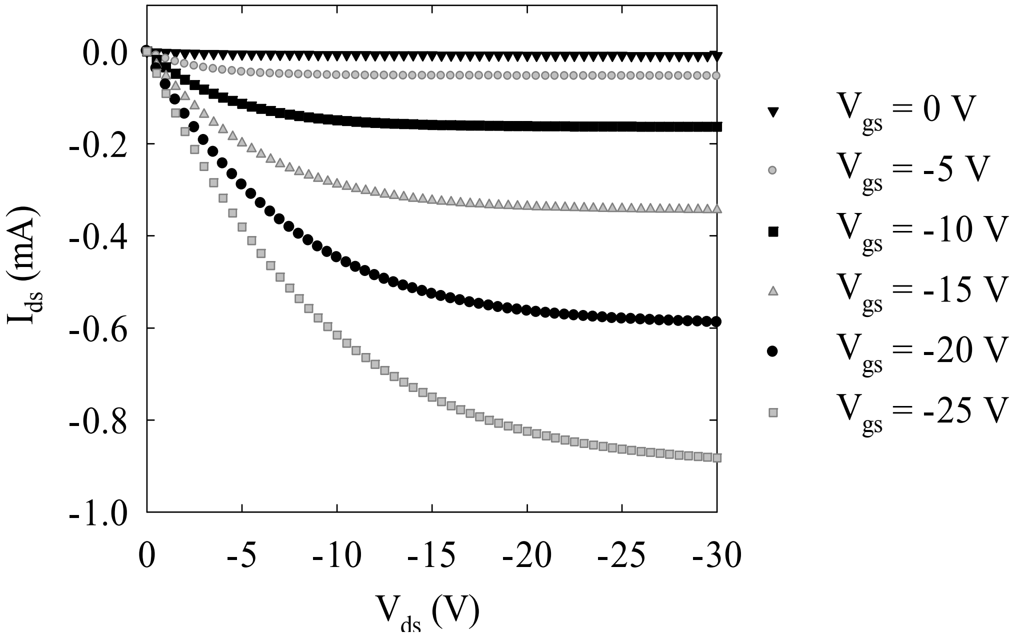

Figure 2.10 Current-voltage characterization for a spin cast diF TES ADT transistor used for voltage modulated reflection measurements at NIST (dielectric 1μm Si_3N_4 .)

2.4 Sample Fabrication

Bottom contact field effect transistors were made with polymer or inorganic insulator as the dielectric layer over a metal gate. I made all samples for electro-optic measurements at the University of Kentucky (cartoon of one transistor is shown in Figure 2.11), and sample structures were made by Oleg Krillov for voltage modulated FTIR measurements at the National Institute of Standards and Technology.

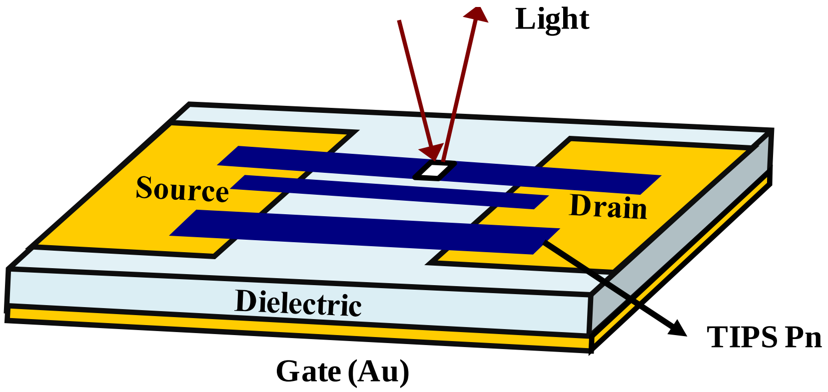

Figure 2.11 Diagram of transistor structure for one set of drain and source contacts, TIPS Pn crystals are shown in dark blue.

2.4.1 Sample structures for electro-optic measurements

Microscope slides are used as the substrate for samples made at the University of Kentucky, and are cleaned by sonicating or heating for ten minutes in each of the following solvents: acetone, ethanol, and de-ionized water, then dried in a stream of nitrogen gas. 20-40 nm of gold or aluminum is evaporated through an aluminum foil mask at a pressure of $5x10^{-5}$ T to form a metallic gate. The dielectric is then applied, as described below in detail (Section 2.5.) Between six and ten gold drain and source contact pairs are evaporated over the dielectric layer through a steel shadow mask or photoresist mask at a distance of 27cm from the evaporation source to limit radiative heating of polymers. Photoresist is used to mask the oxide sample beds to ensure clearer evaporation patterns without blurring edges, which happens when the mask is not flush with the dielectric surface. The steel mask is used with the polymer dielectric to avoid possible damage to the surface from photoresist processing.

The photoresist used to mask is Shipley Microposit S1813 which is coated on the sample by spinning at 3000 rpm for 30 s. After spinning, the photoresist is dried on a

90°C hot plate for 60 s and exposed to UV light through a pattern mask for 10 s. To undercut the photoresist, thereby getting better lift off of the excess metal after evaporation, the sample was then soaked in toluene for 45 s and dried. The photoresist was then developed in Shipley Microposit MF-319 Developer for 30 s and rinsed in deionized water.

2.4.2 Sample structures for charge modulation spectroscopy measurements

Samples measured at the National Institute of Standards and Technology (NIST) for measurements of static voltage modulated FTIR spectra of diF TES ADT transistors were made on polished silica wafers. The gate was optically thick gold over a thin (~5 nm) layer of titanium. Silicon nitride (Si_3N_4) dielectric was deposited by plasma enhanced chemical vapor deposition, followed by the application of gold drain and source electrodes through a photoresist mask. The source and drain contacts were interdigitated in order to achieve a measurement area of ~1 cm^2 without increasing the channel length, as shown in Figure 2.12. Transistor channel length is measured as the distance between two adjacent fingers, and channel width is approximately the length of one finger multiplied by the number of gaps between adjacent fingers. Fingers are 0.05 mm wide and 8 mm long for samples used in this thesis.

Figure 2.12 Cartoon of the interdigitated finger design used in FTIR measurements of voltage modulated reflection; the black circle shows the measurement area.

2.4.3 Semiconductor deposition

Before semiconductor deposition, the sample structure surface is chemically modified to increase transistor performance. First, the sample structure is soaked in a solution of pentafluorobenzenethiol (PFBT) in ethanol (5 mM) for 60 minutes, rinsed in ethanol and dried in a stream of nitrogen gas. During the PFBT soaking process a self assembled monolayer of PFBT is grown on the gold fingers which increases molecular order at the contacts during crystal growth [52,53] and modifies the work function [54,55] of the metal surface, thereby reducing contact resistance [13,56]. Hexamethyldisilane (HMDS) is spin cast on select samples to improve crystallinity and decrease trap states on oxide dielectric surfaces [57-59].

After chemical modification of the surface, the semiconductor is applied. For samples made with TIPS Pn, a 1-2% by weight solution in toluene is applied using a dropper and dried under a cover, the substrate tilted at a slight angle to promote long axis growth along the drain to source direction. Drying the solution under a cover allows extra time for large area crystals to grow; when dried too quickly amorphous or polymorphous films form. For samples made with diF TESADT, a 1-2% solution in chlorobenzene is applied either by drop casting and slow dry (similar to TIPS Pn method) or the solution is spin cast between 500-1000 rpm for approximately 30-seconds.

Electrical contact is made to the drain, source and gate contacts using silver paint to attach leads. Access to the gate is achieved by gently scratching off the dielectric layer.

2.5 Dielectrics

Dielectrics can affect many aspects of an OFET. Below I discuss effects on the electrical performance of the transistor and on the infrared characterization, and give a summary of methods used to deposit thin film dielectrics for this study.

2.5.1 Electrical considerations for the dielectric surface

Electrical effects of the dielectric can affect the quality and performance of the transistor built, as discussed in Section 1.3.1. In addition, physical defects in the dielectric can affect the electrical performance: pinholes can cause leakage current from source and drain contacts to the gate, and the roughness of the dielectric can disrupt the molecular stacking or cause the formation of grain boundaries during OSC deposition [24,60].

Transistor current is normally expected to increase with increasing capacitance, since this should result in increased charge density and lowered operating voltage of an OFET [13]. The capacitance (per area) depends on material properties as:

$$C_{ox} = \frac{\varepsilon\, \varepsilon_0}{d} \qquad \text{Equation 2.3}$$

A thinner insulator (d) or higher dielectric constant (ε) is therefore expected to increase current, but due to the high polarizability of OSC, increasing the dielectric constant does not always increase performance. Increasing the dielectric constant in oxide dielectrics decreases mobility and increases hysteresis and threshold voltage in OFETs suggesting charge trapping on polar functional groups of the oxide [24,61,62]. In contrast to these results on oxides, mobility increase with increasing dielectric constant was seen in cross linked poly-4-vinylphenol (PVP), which was controlled through modifying the PVP:crosslinker ratio [63], though this increase was small and for a small range of ε.

Improvements in electrical performance of OFETs have been achieved by modifying the surface of inorganic dielectrics using thin films of polymers or self assembled monolayers which can smooth the surface, modify the surface energy and surface chemistry (including reducing the number of trap states) [25,64]. This can result in increasing mobility and decreasing threshold voltage; mobility can be increased by a factor of 10 or more [59], though care must be taken in choice of modifying chemical with some precursors causing a decrease in performance [65]. In this study we use HMDS (Section 2.4.3) on select samples.

2.5.2 Optical effects of the dielectric

Measurements using light put additional constraints on the dielectric layer properties.

Buried Metal Layer (BML)

Light reflected off the metallic gate will have a node at the gate; if the semiconductor-dielectric interface is placed approximately λ/4n away from the gate the intensity of light interacting with the active layers can be 3-4 times larger than the average intensity. A simplified schematic is shown in Figure 2.13. Using Maxwell's equations, we have calculated the intensity of light at the dielectric-OSC interface as a function of the dielectric thickness (Figure 2.14.) The ideal dielectric and OSC thickness is affected by the wavelength of the light in the dielectric, the wavelength of the light in the OSC, and the interference effects of reflecting off multiple surfaces. Consequently, the ideal thickness for dielectric films in electro-optic measurements with ν ~ 1000 cm^{-1} and n ~ 2 is ~ 1 μm; electro-optic signal fell below noise levels for transistors with much thinner dielectric films (~ 0.3 – 0.5 μm.)

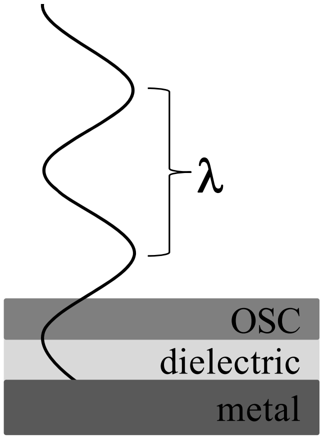

Figure 2.13 Simple schematic showing the buried metal effect, which is used to enhance the interactions of light with the active layer in the semiconductor.

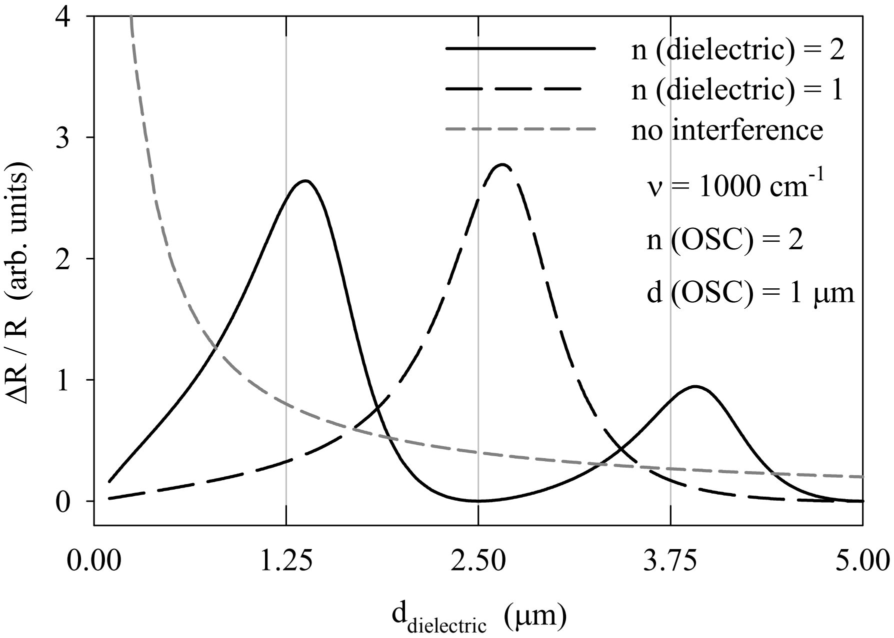

Figure 2.14 Calculation of enhancement of the change in reflectance due to the interaction at the charging interface, influenced by the interference effects in the dielectric and OSC.

Index of Refraction in the Infrared

Many inorganic dielectric materials have phonon modes in the spectral measurement range that cause the index of refraction to vary (Figure 2.15.) For measurements we chose materials with relatively constant index of refraction values in the wavelength range of our measurement. For example when using Al_2O_3 (Figure 2.16) to measure the electro-optic response with the lasers, we focused on measurements around 1000 cm^{-1}, and when using Si_3N_4 (Figure 2.17) in voltage modulated FTIR measurements at NIST we focused on measurements above 1000 cm^{-1}. The polymer dielectric used in this study also had vibrational modes in the range of interest, but did not effect measurements (see Section 3.2) and could be effectively avoided by choosing a wavelength away from the polymer modes (Figures 2.17 and 2.18.)

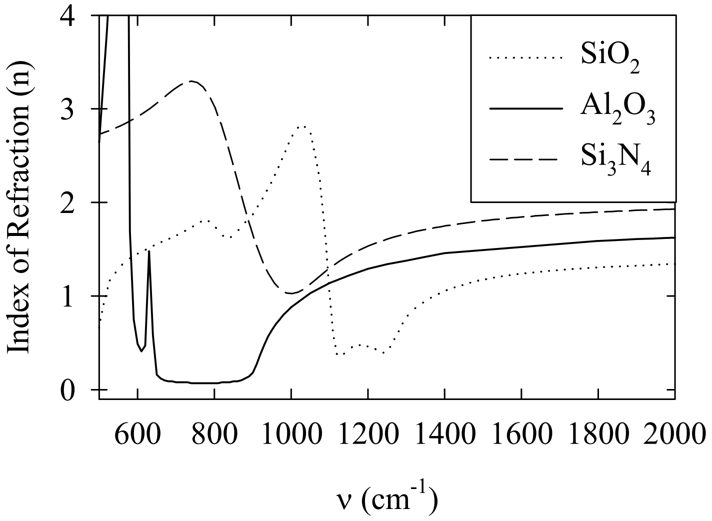

Figure 2.15 Graph of the index of refraction in silicon dioxide, aluminum oxide, and silicon nitride in the infrared. Silicon nitride values were measured at NIST using a spectroscopic ellipsometer; silicon dioxide and aluminum oxide values were obtained from reference [66].

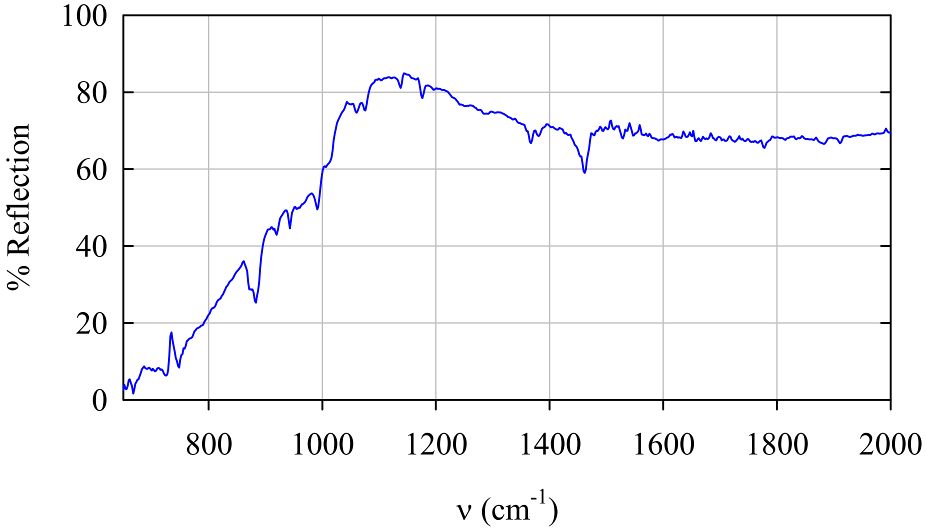

Figure 2.16 Spectrum of TIPS Pn on Al_2O_3 over gold.

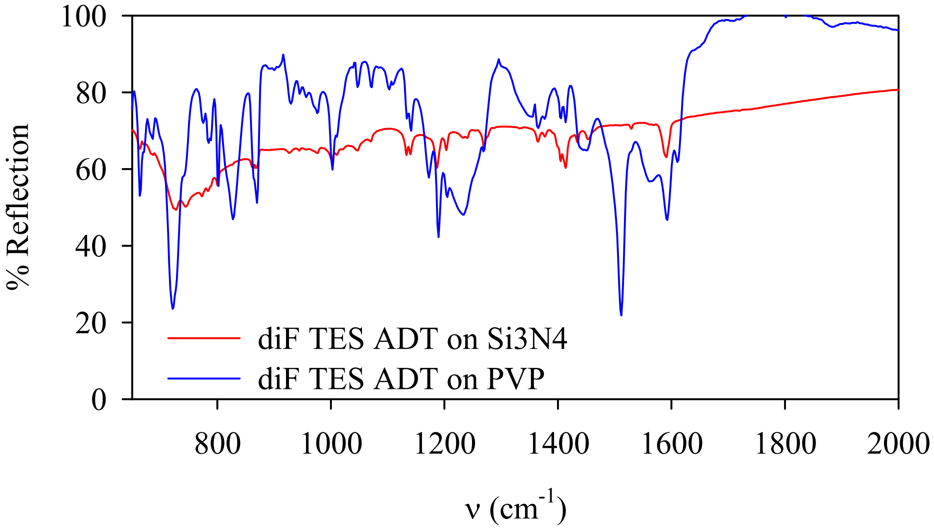

Figure 2.17 Spectra of thin film diF TES ADT on Si_3N_4 and polymer dielectric PVP. Light is reflected off the gold layer and is absorbed in the thin layers.

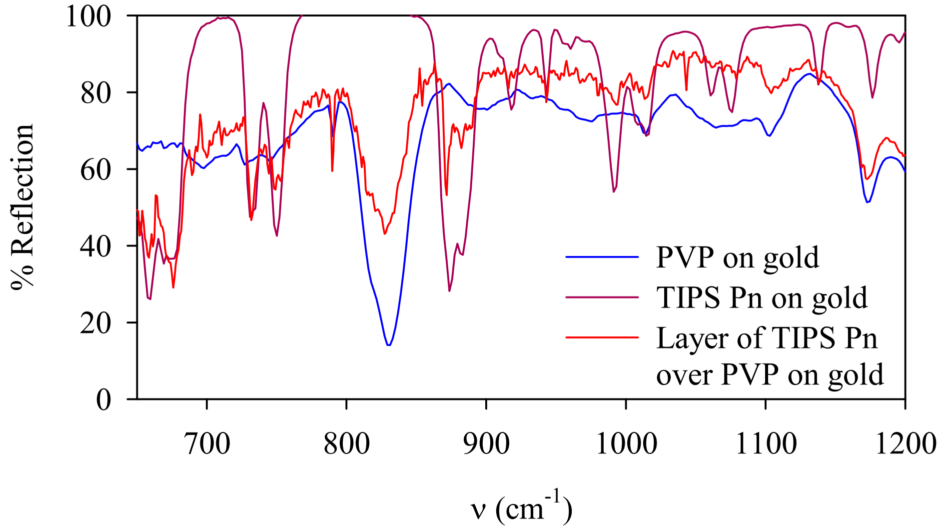

Figure 2.18 Spectra of thin layers of TIPS Pn and polymer dielectric PVP. Light is reflected off the gold layer and is absorbed in the thin layers.

Electro-optic Response of Silica Wafers

Studies of the electrical properties of OSCs will often use doped silicon wafers with polished thermal oxide as the substrate. Although these wafers are convenient, as gate and dielectric are pre made, our measurements of gate voltage modulated IR reflectance show a large dynamic signal, as shown in Figure 2.19, on samples with a thin layer of gold (~ 5 nm, transparent to IR light) substituting for the OSC. We speculate that this signal originates in the movement of charged species on a silica surface or the silicon-silica interface. This signal was also observed on samples where the silica was covered by a 30-40 nm gold gate and Al_2O_3 deposited as the dielectric.

Shown in Figure 2.20 is the electro-optic response of a thin layer of gold covering a PVP dielectric with a gold gate. As expected, the signal is small and persists to high frequency. The signal comes from the excess mobile charge induced by an applied gate voltage, similar to the signal on an OFET, but is not limited in the frequency domain by low mobility as in OFETs (Chapter 4.)

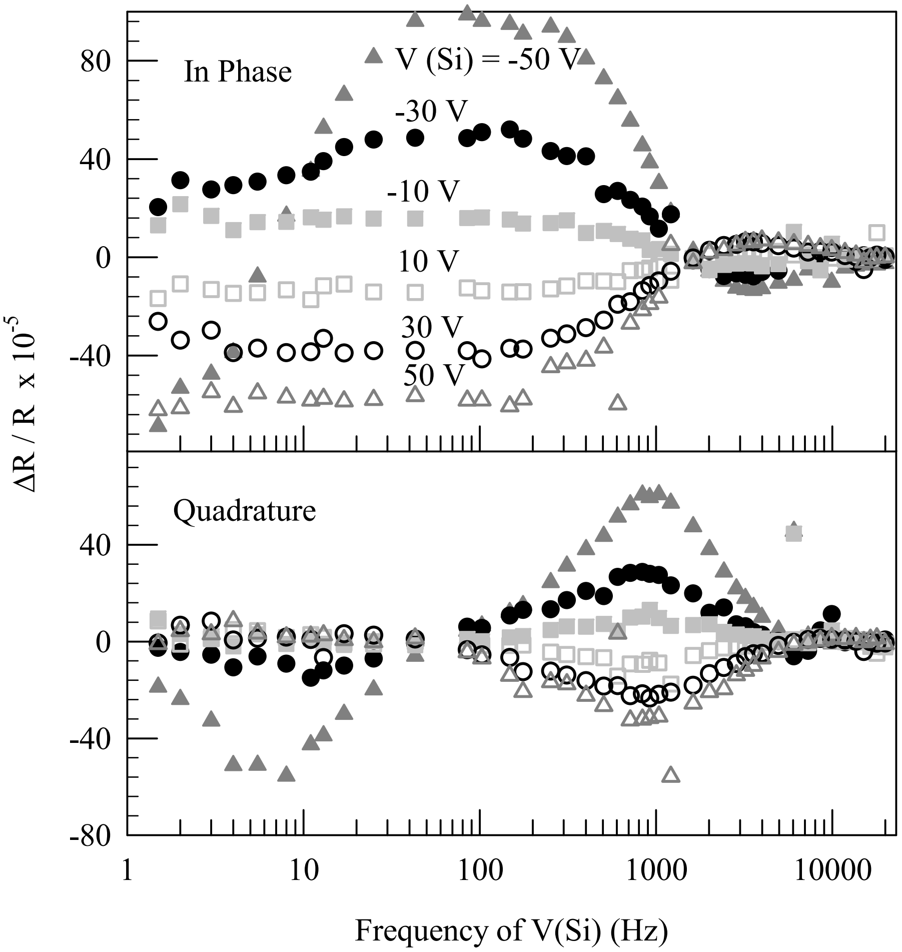

Figure 2.19 The dynamic infrared electro-optic response of a p-doped silica wafer taken at 1000 cm^{-1}. Transistor structure was used to measure the response, where an optically thin layer of gold connected thick source and drain contacts.

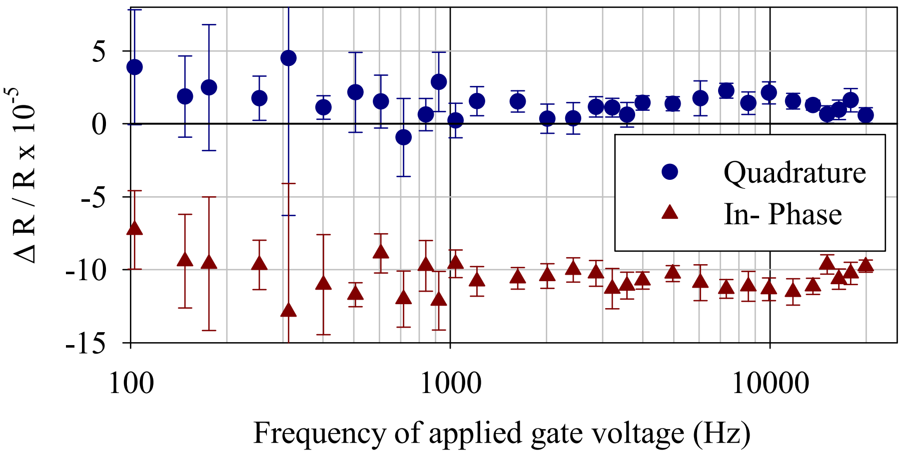

Figure 2.20 The dynamic infrared electro-optic response of a thin layer of gold over PVP dielectric at ν ~ 900 cm^{-1}.

2.5.3 Dielectric deposition and processing

The two methods we use to make the insulating layer of the OFET samples are spin coating a polymer and using atomic layer deposition (ALD) to apply aluminum oxide, Al_2O_3. At NIST insulating layers were prepared by Oleg Krillov using plasma enhanced chemical vapor deposition (PECVD) of silicon nitride, Si_3N_4.

The polymer insulator used was poly-4-vinylphenol (Mw- ca. 25,000) (PVP) cross linked with methylated poly(melamine-co-formaldehyde) 84% wt.% in 1-butanol (MMF) dissolved in propylene glycol monomethyl ether acetate (> 99.5%) (PGMEA) which is spin cast over the gate metal. The thickness of the insulating layer can be controlled by varying the spin speed and the concentration of the PVP/MMF mixture in PGMEA, Figure 2.21. The PVP solution was made with a 1:3 wt% mixture of MMF:PVP, and the final solution concentration was between 10-17% PVP/MMF in PGMEA. The solution is spun between 2000 and 4000 rpm for 30-45 seconds. Better uniformity was attained in our lab using one spin speed, rather than varying the speed in steps. After deposition, the solution was dried at 100°C for 10 minutes and cross linked at 200°C for 10 minutes.

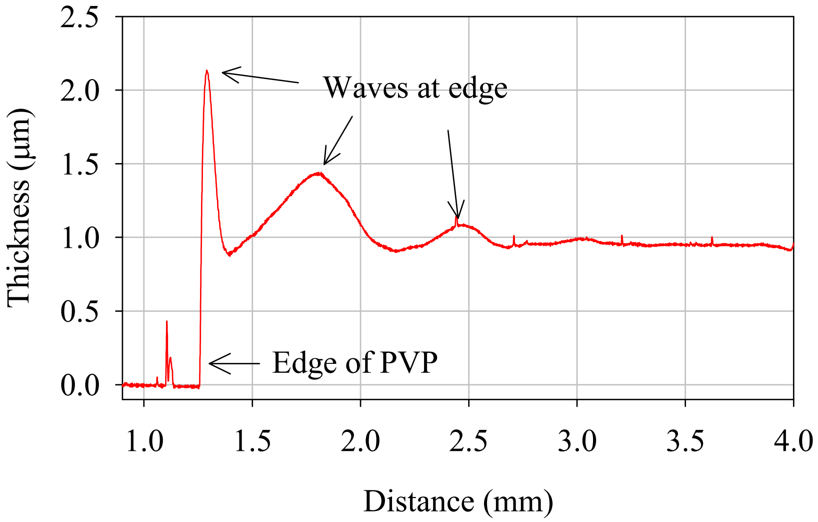

Figure 2.21 Thickness at the edge of a PVP film, measured using a profilometer. Waves form at the edges of the PVP, sample structures are placed far (> 4 mm) from the edge of the PVP to avoid the thickness variation in these areas.

Cross linked PVP films are reported to have dielectric constants ranging from 3.6-6.4 depending on composition and other parameters, such as cross linking temperature

[24,63]. Due to the uncertainty in our capacitance meter, measurements of dielectric constant in our PVP samples varied between 3 and 10 and were therefore assumed to be unreliable. Based on a comparison between composition and procedures used to produce our PVP films and those in literature we chose to use $\varepsilon = 3.6$ for calculations [63].

Variation in PVP dielectric due to composition, smoothness (see Figure 2.21), non ideal OFET IV characteristics (leakage current, bias effects, etc.), and need for higher electro-optic signal (higher charge densities on dielectrics with higher ε), lead us to pursue inorganic dielectrics. We tried many inorganic dielectric deposition methods including chemical vapor deposition, thermal evaporation, electron-beam and sputtering of titanium oxide, silicon oxide, and aluminum oxide. The films we produced were not insulating or had very low (< 5V) breakdown voltage; for example all transistors we prepared with sputtered oxide dielectrics either had pin-holes (large gate leakage currents) or developed them at very small applied gate voltages. A method that produced usable samples was atomic layer deposition (ALD) of Al_2O_3. ALD deposited Al_2O_3 has a high breakdown voltage (5.2MV/cm) and a dielectric constant of $\varepsilon = 7.5$ [67].

ALD provides a smooth and nearly pinhole free dielectric layer due to the sequential, self-limiting reactions that form the thin film. Aluminum oxide, Al_2O_3, was deposited by alternating exposure to trimethylaluminum (TMA) and water in the following sequence in a Savannah ALD system manufactured by Cambridge NanoTech Inc:

1. Exposure to TMA, precursor is chemabsorbed onto the substrate
2. Nitrogen purge of the chamber
3. Exposure to water gas which reacts with the methyl groups to form oxygen bridges, hydroxyl surface species, and methane gas
4. Nitrogen purge of reaction gases in the chamber

To deposit aluminum oxide films, the substrate is placed in vacuum at 200°C with a nitrogen gas purge set at 20 sccm. Al_2O_3 is deposited through this reaction at a rate of 0.11 nm/cycle, each cycle takes approximately 8 seconds to complete. ALD deposition of 1-2 microns of Al_2O_3 required over 24 hours of deposition time. Due to this, depositions were run overnight on shared equipment in the CeNSE center and were done over several nights, with the samples being taken out of the chamber every 14 hours for ~ 8 hours. Approximately 750 nm of Al_2O_3 can be deposited in one run.

We chose to use Al_2O_3 instead of silicon dioxide due to the thickness requirements of our experiment, as silicon dioxide reactions require a much longer (~30 second) exposure and purge times per layer. Additionally, as shown in Figure 2.19, SiO_2 may have a large, parasitic electro-optic response.

CHAPTER 3 **Voltage Modulated Infrared Measurements of TIPS Pn and diF TES ADT: Spectral and Spatial Dependences**

3.1 **Introduction**

Charge conduction in small molecule organic semiconductors is associated with the delocalized carbon π-bonds, which have vibrational energies in the 1100 - 1700 cm^{-1} range for materials like pentacene and diF TES ADT [68]. Applied electric fields or excess charge on a molecule will cause electric dipole changes in the molecules which result in changes to the molecule vibrational and rotational energies [69]. For example, the signature vibrations (including hydrogen wagging) between 700-1500cm^{-1} in pentacene shift 10 - 30 cm^{-1} when the molecule is ionized, with highest sensitivity closest to the CC bonding energies [70,71].

In addition to molecular vibrational energies, polarons formed in polymer organic semiconductors also have energies in the infrared range. Li et al. [7]. observed the formation of polarons and infrared active vibrational modes in poly(3-hexylthiophene) when a gate voltage was applied, and observed that the IR spectral weight of these features is proportional to the density of carriers. In highly ordered systems it is not clear if polarons exist, as discussed in Section 1.4. In single crystal rubrene for example, polarons are not observed, though broad-band absorption of light in the mid to far infrared was observed in the "on" state ($V_{gs} < 0$) [6] suggesting that at low enough frequencies the extra charge induced is able to absorb light, possibly due to delocalization of the charge carriers over several molecules [28].

In order to gain insight into the nature of charge transport in TIPS Pn and diF TES ADT we studied the gate voltage modulated absorption spectra in the mid infrared. TIPS Pn and diF TES ADT both show a broadband absorption in the 425 – 1100 cm^{-1} range; additional studies in the 1000 – 1600 cm^{-1} range for diF TES ADT show changes in vibrational energies.

Our measurements of infrared light absorption through organic transistors in the 425 – 1100 cm^{-1} range can be used to probe the local charge density in the low frequency (static) case and for dynamic charging with a spatial resolution of 20 microns. The charge distribution between the drain and source of an OFET changes with applied gate, drain and source voltage, and can be affected by contact resistance, grain boundaries, and impurities. Scanning Kelvin probe microscopy has been used to evaluate the voltage within the channel: across grain boundaries[72], at the contacts, and around impurities [26]. Visible light has been used to probe the static charge in a working pentacene field effect transistor [8], and second harmonic generation has been used to measure the dynamics of charge moving from source to drain [21]. Our infrared measurements show that the charge distribution is constant at low frequencies for typical samples and show variation for higher frequencies as expected.

3.2 Charge induced infrared absorption

In our lab, the best sensitivity is obtained using AC measurements using our lasers as discussed in Section 2.2, which limits our spectral range but increases our spatial resolution. When measuring the "static" charging, we performed low frequency measurements (typically 500 - 700 Hz), well below the characteristic frequency of the transistor. Using a standard OFET configuration, we apply a square wave gate voltage (V_{gs}) to the sample while measuring the reflection off of the gold gate for measurement areas of around 30 μm x 30 μm. To get spectral dependence, the wavelength of the laser light is varied from low to high wavenumber and measurements are taken at one location between drain and source.

Measurements were made on drop cast samples of TIPS Pn and diF TES ADT on polymer (PVP) or aluminum oxide (Al_2O_3) dielectric on structures described in Section 2.4.1. Crystals used for measurement made contact with the source and drain electrode, and showed current response to gate voltage in IV characteristics.

Results

When a negative voltage is applied to the gate, positive charges are induced onto the bottom layers of OSC closest to the gate. If the charges are not trapped or tightly bound to molecules, the charges will be mobile and absorb light. Figures 3.1 and 3.2 show the absorption of light in OFETs made with TIPS Pn and diF TES ADT, respectively. The broadband signal is due to the change in conductivity in the semiconductor caused by the introduction of mobile charges when applying a gate voltage (see Section 1.5.2.) The amount of absorption though a thin layer of charge can be roughly estimated using Equation 1.6, which assumes the low conductivity limit for mobile charges, and the values relevant for the TIPS Pn transistor on PVP dielectric obtained from IV measurements: mobility $\mu_{lin} = 0.06\ cm^2/Vs$, $\varepsilon \approx 3.6$, dielectric thickness $d = 1\ \mu m$, and the two-dimensional charge density $\rho_{2D} = \varepsilon\varepsilon_0 V_{gs}/d$. This estimate, $\frac{\Delta R}{R} \approx -5\times10^{-6}$, is ten times lower than measured data shown below. The buried metal layer effect will enhance the absorption by a factor of 3 – 4 (Figure 2.14.)

The energy range of the lasers covers the resonant energy of hydrogen wagging bonds in TIPS Pn (and related materials), which are assumed to have a low involvement with mobile charge as compared with delocalized C=C bonds. In cations of pentacene, charge-induced shifts of 10 – 30 cm^{-1} are observed for the CH out of plane wagging, which fall in the 600 – 1000 cm^{-1} range [71], but we do not observe energy shifts of the molecular bonds with applied voltage in this region for TIPS Pn (Figure 3.1, Figure 3.2.) From the magnitude and width of the reflectance spectral features, and assuming that the crystal is ~25 molecules thick, our noise level $\Delta R/R \sim 10^{-5}$ suggests that the phonon frequencies change less than 4 cm^{-1} with charging. Alternatively, the lack of spectral anomalies may be an indication that charges in the surface layer hop between molecules in times less than the phonon periods, or are delocalized over several molecules.

3.2.1 A note on sample age and performance

We measured the voltage modulated spectra for both TIPS Pn and diF TES ADT transistors. Both show absorption of light over the wavelengths measured, though in diF TES ADT this signal decreases by four when the sample is stored for one month (Figure 3.2.) TIPS Pn does not show this same degradation, though it was also stored and measured in air.

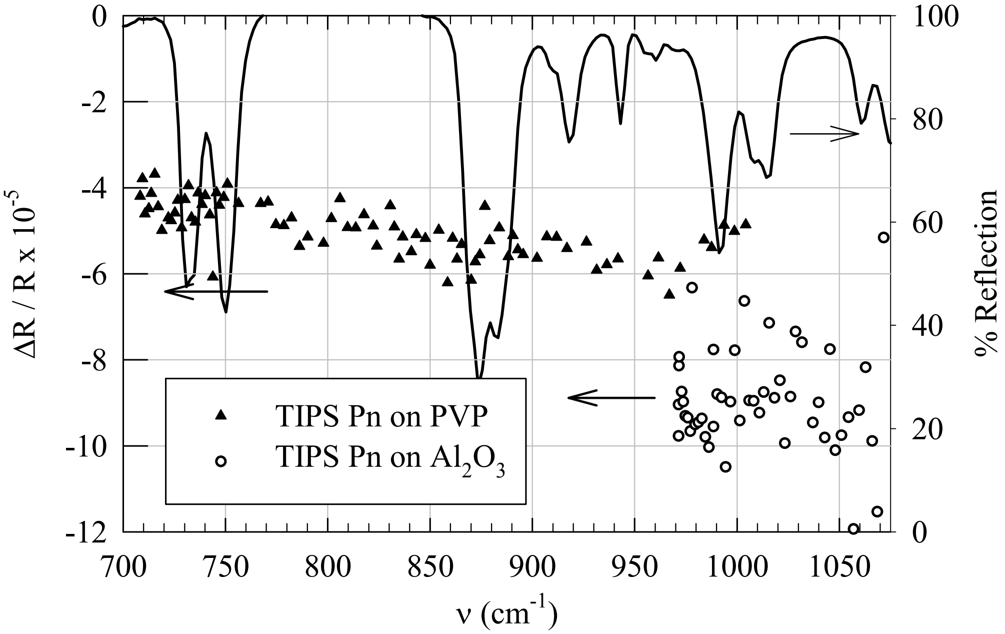

Figure 3.1 TIPS Pn Reflection and electro-optic spectra. Reflectance spectrum of a TIPS Pn on gold is shown in the black line, axis on right. Black triangles show the electro-optic spectrum of TIPS/PVP Sample 1. Applied square wave voltage was V_{gs} = -50 V at 714 Hz. Black circles show the spectrum of TIPS/Al_2O_3 Sample 2, V_{gs} = -100 V at 505 Hz.

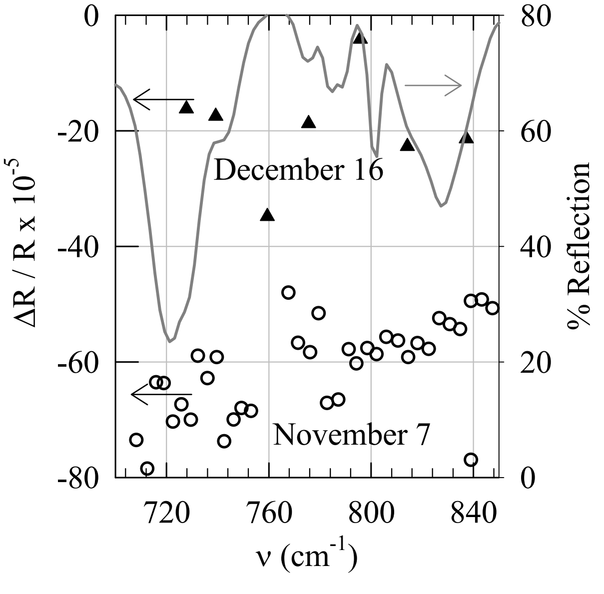

Figure 3.2 diF TES ADT electro-optic and reflection spectra (grey, axis on right) for FTES/PVP Sample 1. A large decrease in electro-optic signal (triangles and open circles, axis on left) is seen after a month in storage.

3.3 Voltage dependence of the charge density

For a typical sample at low frequency (well below the characteristic frequency) and drain to source voltage $V_{ds} = 0$ the electro-optic signal varies linearly with the gate voltage at all points along the transistor channel. Figure 3.3 shows signal variation as V_{gs} is increased, voltage is applied at a frequency of 505 Hz for TIPS/PVP Sample 1. The linear dependence shows the capacitive charging of the transistor.

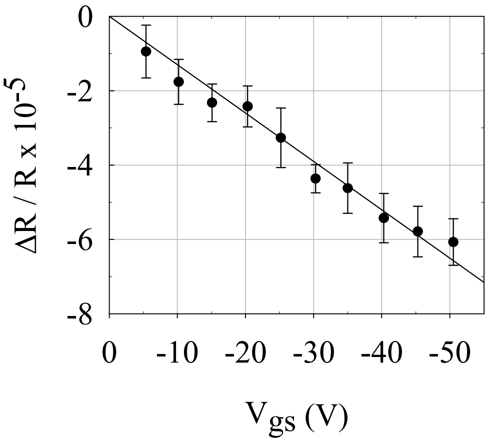

Figure 3.3 Electro-optic signal for a TIPS Pn transistor, TIPS/PVP Sample 1, as a function of gate voltage with drain and source grounded. Signal was measured at the center of the FET channel, and voltage was applied at a frequency of 505 Hz.

3.4 Charge distribution in TIPS Pn transistors

We use the broad-band infrared absorption described in Section 3.2 to measure the distribution of charge within our TIPS Pn and diF TES ADT samples (diF TES ADT samples are presented in Section 4.7.) The microscope is used to focus light into a $\sim 20\ \mu\text{m} \times 20\ \mu\text{m}$ measurement area that is moved from drain to source, taking measurements at $\sim 25\ \mu\text{m}$ intervals. TIPS Pn transistors on PVP dielectric show no spatial dependence of the ΔR/R signal from drain to source at low frequency (Figure 3.4) when gate voltage is applied and drain and source are held at ground. Figure 3.4a shows data for a sample with constant voltage applied to the gate, and voltage applied to the drain at low frequency (~static).

When applying a drain to source voltage (ie with $V(L) = V_{dg} = 0$ and $V_{sd} = V(0) \neq 0$) the static case of Equation 1.9 gives (also shown by Manaka et al. [8].)

$$\rho(x) = CV_{sd}\sqrt{1 - \frac{x}{L}}$$ Equation 3.1

Figure 3.4b shows this case, and data fits Equation 3.1 within noise.

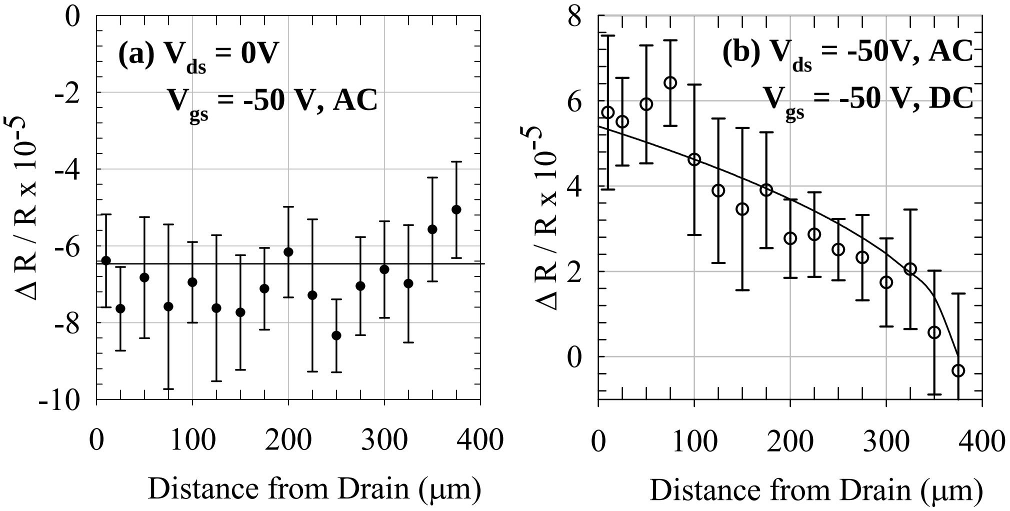

Figure 3.4 Voltage modulated reflection measured in-phase with the applied gate voltage (714 Hz) on TIPS/PVP Sample 1. Signal measured using ~ 907 cm^{-1} light positioned on a crystal within the FET channel. (a) AC voltage is applied to gate only, drain and source held at ground. (b) DC voltage is applied to the gate while AC voltage is applied to the drain. Fit to Equation 3.1 is shown.

When applying a gate voltage at higher frequencies, the position dependence of the charge density will vary based on how fast the charge can reach each area of the transistor. As noted in Section 1.6 and by Matsui and Hasegawa [5] the charge will decrease toward the center of the channel as the frequency of the gate voltage approaches the characteristic frequency of the transistor. In-phase and quadrature measurements show the charging and discharging dynamics, as seen in Figure 3.5. For this TIPS Pn sample made with Al_2O_3 insulator (TIPS/Al_2O_3 Sample 2), there is constant in-phase signal across the transistor and no quadrature signal at low frequency; as the frequency increases the in-phase signal decreases and the quadrature signal increases, showing a delay in charging. Higher frequencies (shown in Chapter 4) can result in inversion of both in-phase and quadrature signals- as expected for an overdamped oscillator.

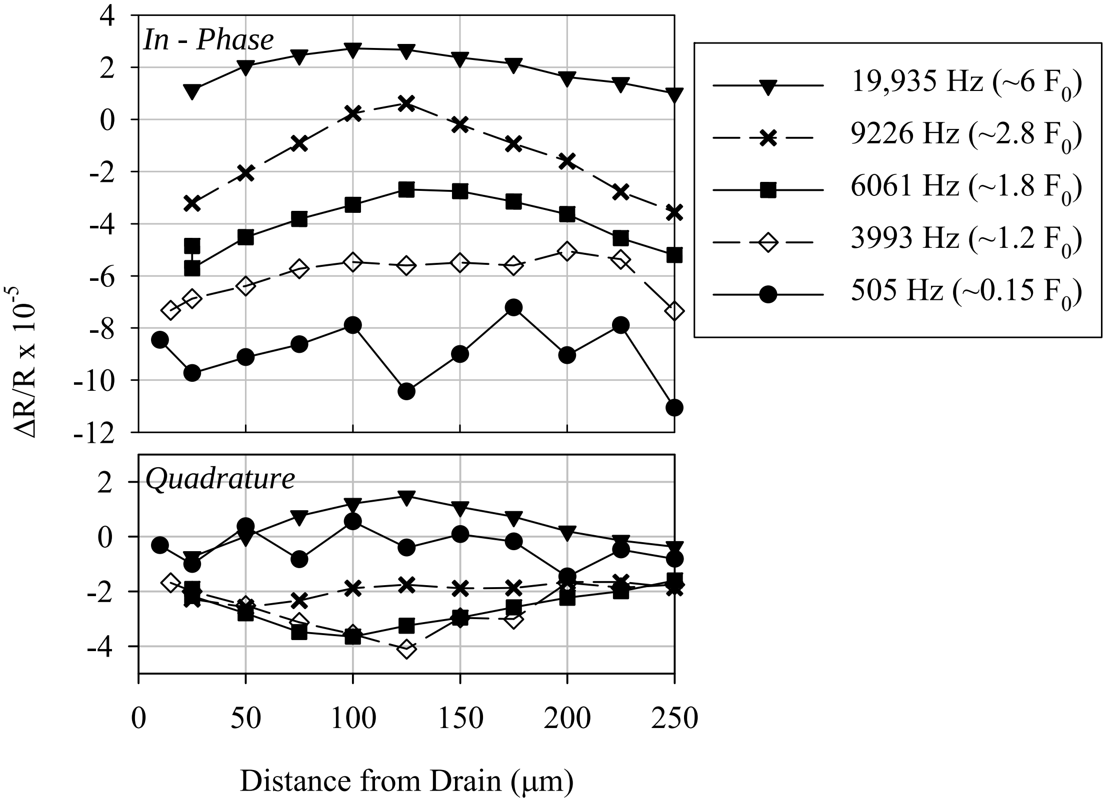

Figure 3.5 Spatial dependence of the change in reflection measured for various frequencies on a TIPS Pn sample (TIPS/Al_2O_3 Sample 2) with alumina gate dielectric. F_0 is the characteristic frequency of the transistor.

3.5 Vibrational energy shifts in diF TES ADT

Voltage modulated spectra can be taken for a broader set of wavelengths when the FTIR is used. In order to obtain a good signal to noise ratio, a larger area (~1 cm^2) transistor is necessary for FTIR measurements. In addition, AC measurements (which take advantage of the signal filtering of lock-in amplifiers) are not possible since the frequency of applied voltage should be much larger than $F = 2v\nu$, where v is the mechanical velocity of the interferometer mirror and ν is the wavenumber [73]. This pushes the gate voltage frequency to well above 3,600 Hz (for typical values of v = 1.9 cm/s and ν = 900cm^{-1}), which is comparable to the characteristic frequency of the transistor.

Measurements of voltage modulated FTIR spectra were performed on diF TES ADT crystals prepared by drop casting or spin casting onto transistor structures with interdigitated drain and source contacts on Si_3N_4 dielectrics prepared with or without surface modification by HMDS or PFBT monolayers, as described in Section 2.4. Chemical modification of the surfaces produced no discernible effect on the voltage dependence of phonon frequencies, though the method of OSC deposition (spin casting versus drop casting) produced different effects. The measurement technique using the FTIR at NIST is described in Section 2.1.4.

Results

Drop cast diF TES ADT samples show changes in vibrational frequencies of phonons in the 1100 - 1600 cm^{-1} range due to the application of gate voltage, as seen in Figure 3.6. The vibrations around 1200 cm^{-1} are unidentified, though most likely are single bond vibrations; 1403 cm^{-1} and 1413 cm^{-1} are C=CH bending; and the vibration at 1588 cm^{-1} is the C=CF stretch at the ends of the molecule (see Figure 1.1) [68]. The close spacing of the modes around 1200 cm^{-1} and 1400 cm^{-1} makes voltage modulated changes in individual modes difficult to interpret, though it is obvious that the magnitude of the changes increase with applied voltage. The C=CF stretch at 1588 cm^{-1} shifts up in energy under increased gate voltage, as seen in the derivative shape in Figure 3.6.

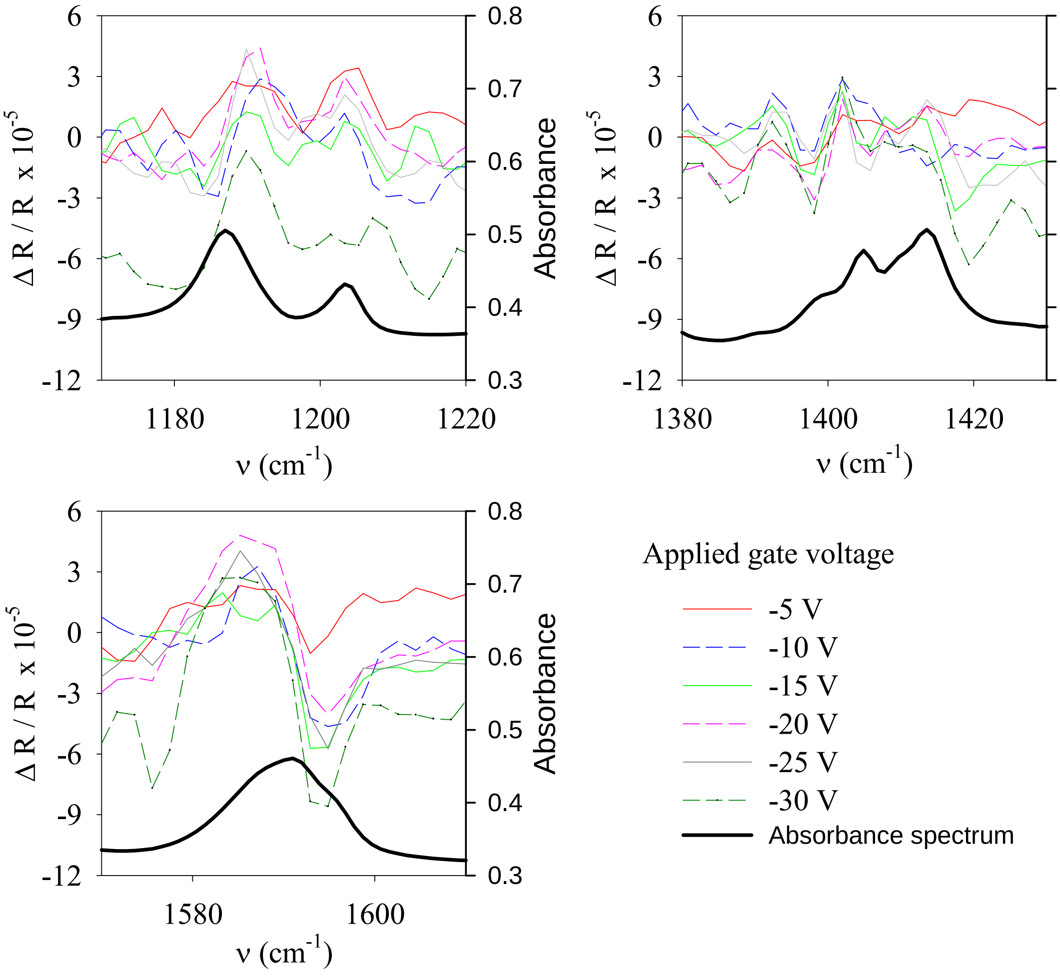

Figure 3.6 Voltage modulated IR spectrum of a drop cast diF TES ADT sample. Due to drift in FTIR data taken over many hours, the data is plotted minus the average value of the total data set.

Spin cast samples of diF TES ADT show a different voltage modulated spectral dependence. As seen in Figure 3.7, the spin cast samples show a broad peak response to applied voltage. In addition to the broad signal the spin cast samples also show possible infrared active modes around 1800 – 2100 cm^{-1} and around 1500 cm^{-1}. We were unable to identify the origins of these effects, though we can consider a few possible explanations: the unidentified modes may be due to the increased number of grain boundaries in the spin cast samples, which cause increased defect trapping [74]; the large spectral response in the spin cast films may be due to the large electric fields across the numerous grain boundaries present in spin cast films [72].

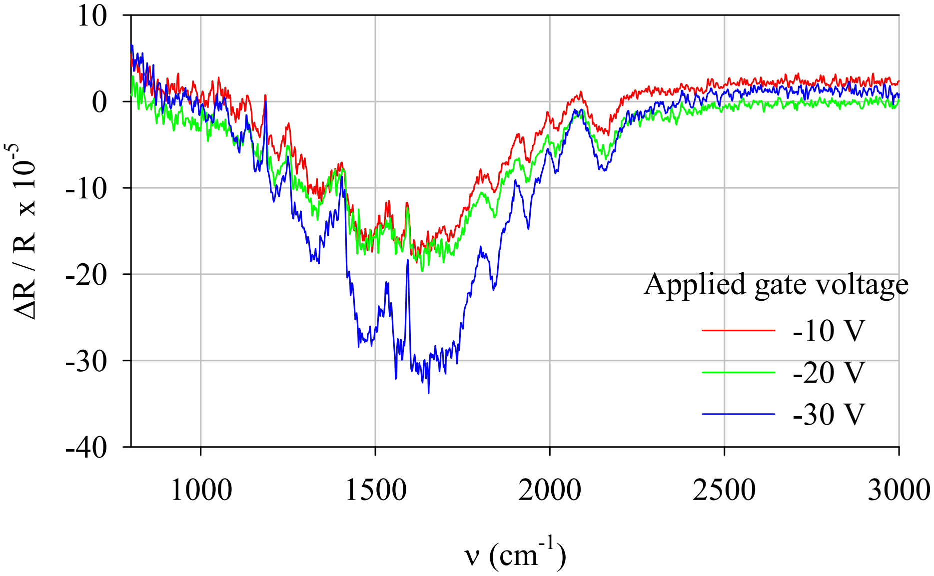

Figure 3.7 Voltage modulated IR spectrum of a spin cast diF TES ADT sample. Due to drift in FTIR data taken over many hours, the data is plotted minus the average value of the total data set.

3.6 Summary

We show that applying voltages to organic semiconductor thin film transistors causes a change in the infrared absorption through the semiconductor material. TIPS Pn and diF TES ADT both show broadband absorption in the range of our lasers (425 – 1150 cm^{-1}), owing to the introduction of positive charges from the drain and source contacts when a negative gate voltage is applied. This signal varies linearly with applied gate voltage due to the capacitive charging of the transistor, and decreases rapidly with age in diF TES ADT samples. Changes in infrared absorption while modulating the gate voltage on a field effect transistor were used to map the charge distribution within the active channel. The charge distribution is constant on TIPS Pn samples at low frequency and decreases toward the center as the frequency of applied voltage increases. Voltage modulated spectral measurements of diF TES ADT show possible differences in charge transport or impurity capture for polycrystalline versus single crystal samples.

CHAPTER 4 **Charge Dynamics in Organic Field Effect Transistors**

4.1 **Introduction**

Reflecting the growing interest in developing devices using organic semiconductors and in understanding their properties, probes are being developed that can measure the dynamic dependence of semiconductor properties within the channel of thin-film field effect transistors. Optical probes have been used to measure the distribution and dynamics of charge in the channel [5,7,8,16,21,75,76] and are going beyond the usual “lumped impedance” approximation of the field-effect transistor (FET.)

Current-voltage measurements suffer from the influence of non-Ohmic resistance at the source and drain contacts, which can vary with temperature and voltage, and the presence of charge traps. There is work toward modifying the interpretation of current-voltage measurements to produce reliable results [77], though more direct routes toward understanding the intrinsic mobility have been investigated that would give more reliable measurements. Measurements like time-of-flight [13] can give reliable measurements of bulk mobility, but do not measure the mobility under high current density and surface influenced measurements that are likely to be seen in working thin film devices made with OSCs. Direct imaging of the electric field using Second Harmonic Generation [21] or the potential profile using scanning Kelvin probe microscopy [4] have been used to give a direct measure of the local mobility in transistors.

In this study, we use spatially resolved voltage modulated infrared reflection to measure the dynamic response of charge in field effect transistors. Specifically, we measure the time it takes for the conducting channel to form after applying a gate voltage to the thin film transistor. We find that this dynamic signal can be used to measure the linear mobility of the device under working conditions, without knowledge of the capacitance or charging, and can be found locally within the transistor channel. Results are compared to the model of dynamic response introduced in Section 1.6, and we investigate the difference in transport between two dielectrics, the variation of mobility within one transistor, and samples with unusual signal.

4.2 Experimental details

To gain information on the charging dynamics of the TIPS-pentacene transistor, a unipolar square wave voltage is applied to the gate, and we measured the relative change in reflectance, ΔR/R, both in-phase and in quadrature with the square wave, as functions of position (x), amplitude (V_{gs}), and frequency (F) using electro-optic techniques described in Section 2.2. Reflection off the gate material means the change in reflection, $\Delta R = R(V_{gs}) - R(V_{gs} = 0)$, is negative when light is absorbed in passing through the active material.

Samples for this study are TIPS Pn or diF TES ADT drop cast on transistor structures with either polymer (PVP) or aluminum oxide (Al_2O_3) dielectric, as described in Section 2.4.

4.3 Measuring mobility using dynamic measurements

By varying the frequency of the gate voltage and measuring the electro-optic response within the channel we can obtain information on the dynamic response of the charge carriers. At the center of the channel, where the charge will travel from both contacts in approximately the same amount of time, we can determine the speed at which the charge can travel half the distance of the channel and use this to estimate the mobility. By using the dynamic response, we do not need knowledge of the capacitance, current or width of the channel, which are needed to extract mobility from IV curves.

Data is compared to the one-dimensional conductor model described in Section 1.6 by fitting a rational expression to the numerical, frequency dependent solution to Equation 1.9, which is plotted in Figure 1.10:

$$\frac{\rho_F(L/2)}{\rho_0} = \frac{\alpha-\gamma z+\varepsilon z^2}{1-\beta z+\delta z^2}, \text{ with } z \equiv \ln\left(\frac{F}{F_0}\right) = \ln\left(\frac{2FL^2}{\mu V_{gs}}\right) \qquad \text{Equation 4.1}$$

where F is the frequency of the applied voltage, ρ is the charge density, L is the length of the channel, μ is the mobility and V_{gs} is the applied gate voltage. The parameters for the in-phase and quadrature response are given in Table 4.1. For comparison to the data, Equation 4.1 can be rewritten as:

$$\frac{\Delta R}{R}\left(x=\frac{L}{2},F\right)=A\frac{\alpha-\gamma\ln\left(\frac{F}{F_0}\right)+\varepsilon\left[\ln\left(\frac{F}{F_0}\right)\right]^2}{1-\beta\ln\left(\frac{F}{F_0}\right)+\delta\left[\ln\left(\frac{F}{F_0}\right)\right]^2} \qquad \text{Equation 4.2}$$

The fitting parameters are the characteristic frequency (F_0) and the overall scale (A.) F_0 is used to find the mobility and is defined as:

$$F_0 \equiv \frac{\mu V_{gs}}{2L^2} \qquad \text{Equation 4.3}$$

In calculations the overall scale A corresponds to the charge density, though this cannot be applied to fits due to the nature of the measurement where the unitless factor ΔR/R is dependent upon both the charge density, ρ_0, and light interference in the OSC and dielectric (see Section 2.5.2.)

Table 4.1 Parameters of Equation 4.1 and Equation 4.2 for the in-phase and quadrature response

	in-phase	quadrature
α	0.3561	0.2541
β	0.3174	0.5293
γ	0.3375	0.3513
δ	0.1448	0.3202
ε	0.06726	-0.01693

The frequency response of the voltage modulated reflectance signal measured near the drain contact and at the channel center of a TIPS Pn transistor made on 1.5 μm thick PVP dielectric is shown in Figure 4.1 (TIPS/PVP Sample 1.) The square wave voltage applied to the gate alternated between zero and -50 V, and the channel length L = 0.4 ± .01 mm. The difference in response between the two positions is due to the time for the charge to move from the contact to the center. Near the contacts the frequency dependence is expected to be position dependent and is therefore affected by the finite size of the light spot, but this is not so near the center, as discussed in Section 1.6. Data at the center is fit to Equation 4.2, A = 1.6 x 10^{-4} and F_0 = 575 ± 50 Hz which gives a mobility $\mu = 0.037 \pm 0.005$ cm^2/Vs. This is within error of the linear mobility from IV measurements (shown in Figure 4.2), $\mu_{lin} = 0.05 \pm .01$ cm^2/Vs, showing the validity of the fit.

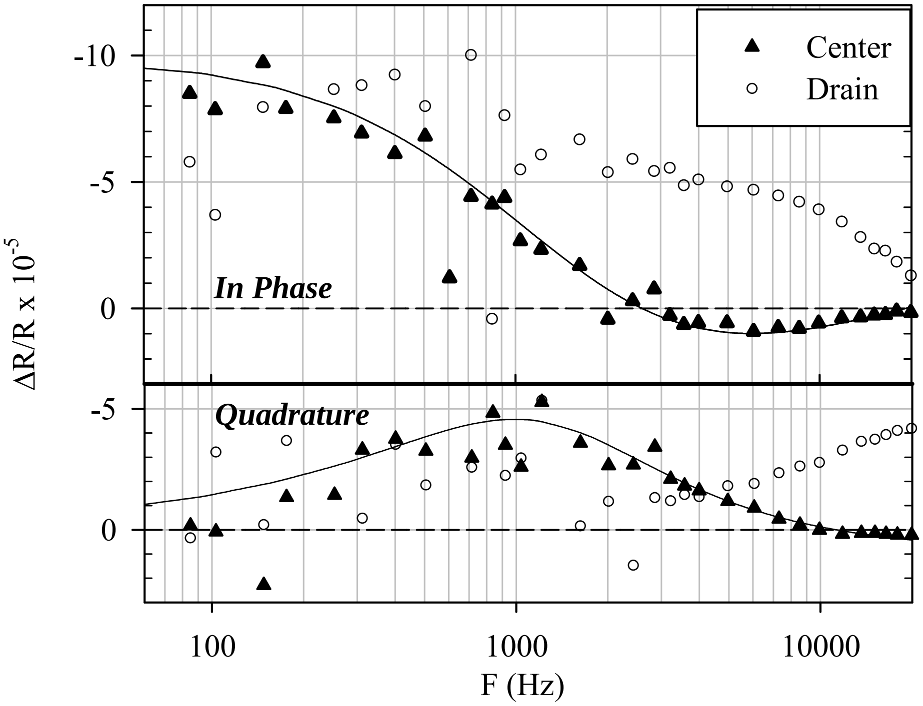

Figure 4.1 Gate voltage frequency dependence of the change in reflectance at the center and near the drain contact on TIPS/PVP Sample 1. Fits of the data at the center of the channel to Equation 4.2 are shown.

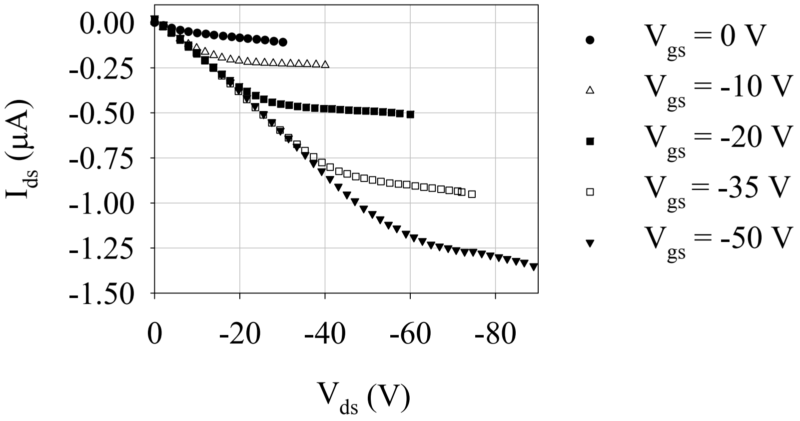

Figure 4.2 Current-voltage measurement for transistor TIPS/PVP Sample 1.

All TIPS Pn transistors with PVP dielectric that we measured show similar behavior; another example (TIPS/PVP Sample 2) is shown in Figure 4.3. Fit of Equation 4.3 to electro-optic data taken at the center of the channel gives $F_0 = 540$ Hz and a mobility of 0.03 cm^2/Vs. Current-voltage data (Figure 4.4) gives a mobility value of 0.02 cm^2/Vs.

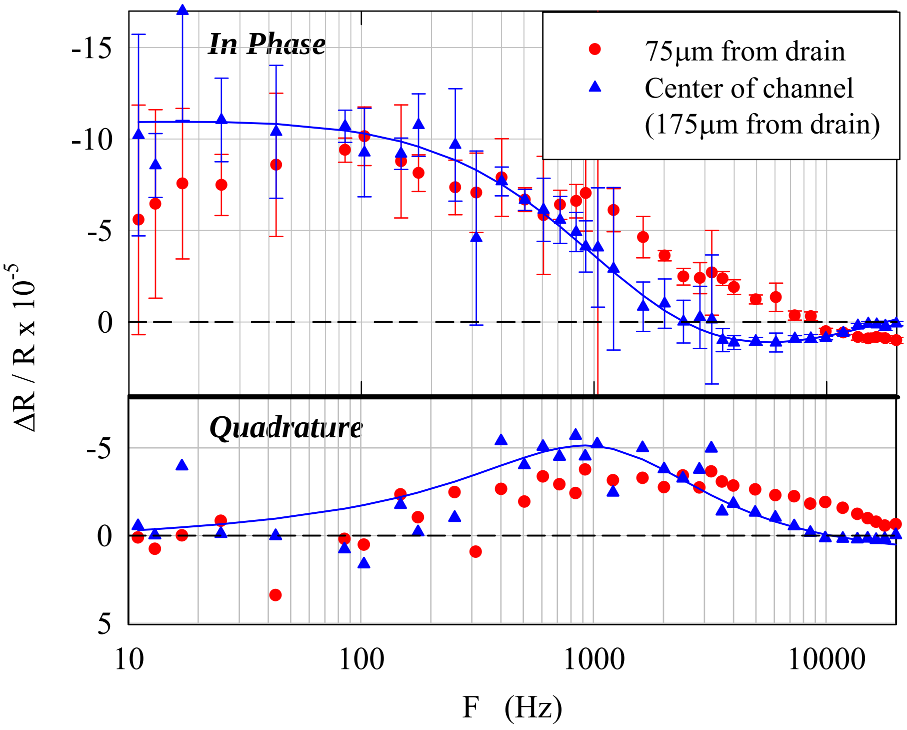

Figure 4.3 Gate voltage frequency dependence of the change in reflectance at the center and 75µm away from the contact on TIPS/PVP Sample 2. Fits of the data at the center of the channel to Equation 4.2 are shown.

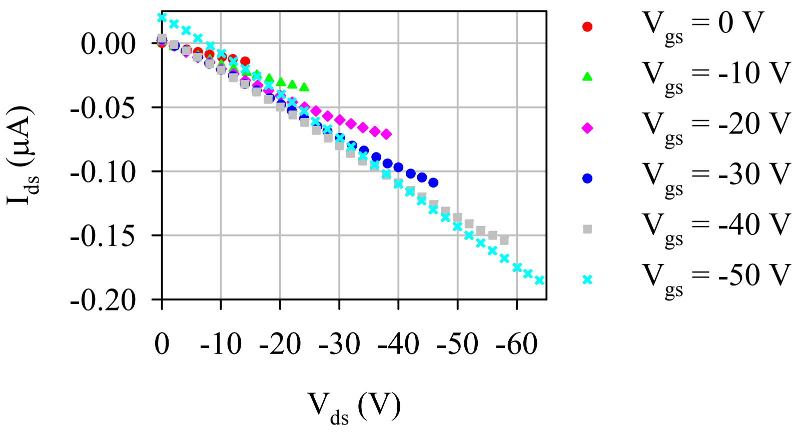

Figure 4.4 Current-voltage characteristic of sample shown in Figure 4.3, TIPS/PVP Sample 2.

4.4 Aluminum oxide dielectric

Using a higher ε dielectric such as aluminum oxide can provide a higher capacitance, resulting in higher charge density for a given gate voltage. In pursuing Al_2O_3 as a gate dielectric, we hoped to obtain a larger and cleaner electro-optic signal. Samples made on glass slides, as described in Section 2.4, provided clean signal at V_{gs} = -25 to -100 V, and on some samples, signal was doubled as compared with PVP dielectric.

The IV characteristics and frequency dependence of the ΔR/R signal for TIPS Pn samples prepared on Al_2O_3 dielectric (TIPS/Al_2O_3 Samples 1 and 3) are shown in Figures 4.5, 4.6, and 4.7. On samples prepared on Al_2O_3, the change in reflectance with frequency deviates from the calculated charge density at high frequency (above 6kHz), though the current-voltage data is similar to what is obtained for PVP dielectric. The mobility values extracted from the data still show correlation with the mobility values from current-voltage data, though IV values always are lower by ~ 0.01 - 0.03 cm^2/Vs. For the data in Figures 4.6 (Sample 1) and 4.7 (Sample 3), mobilities from electro-optic data are 0.03 cm^2/Vs and 0.07 cm^2/Vs respectively, and the corresponding IV data gives 0.02 cm^2/Vs and 0.06 cm^2/Vs.

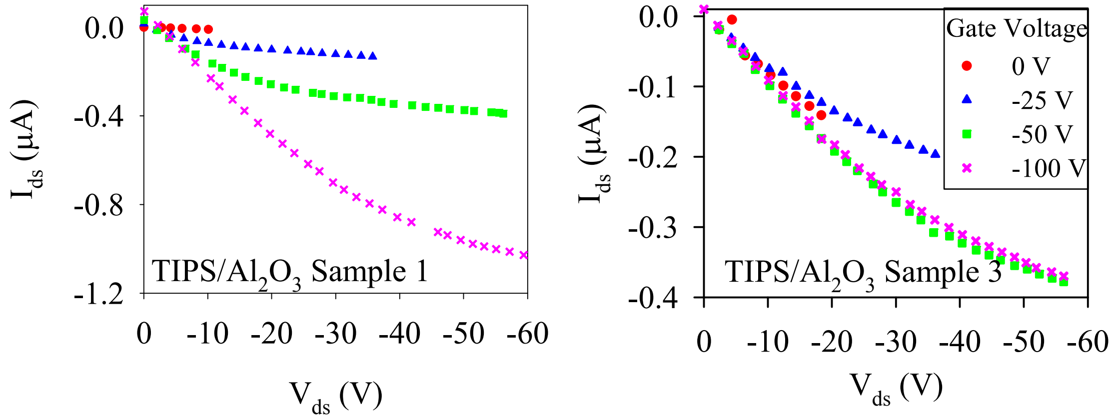

Figure 4.5 Current-voltage data for TIPS/ALD Samples 1 and 3. Legend on Sample 3 data applies to both graphs.

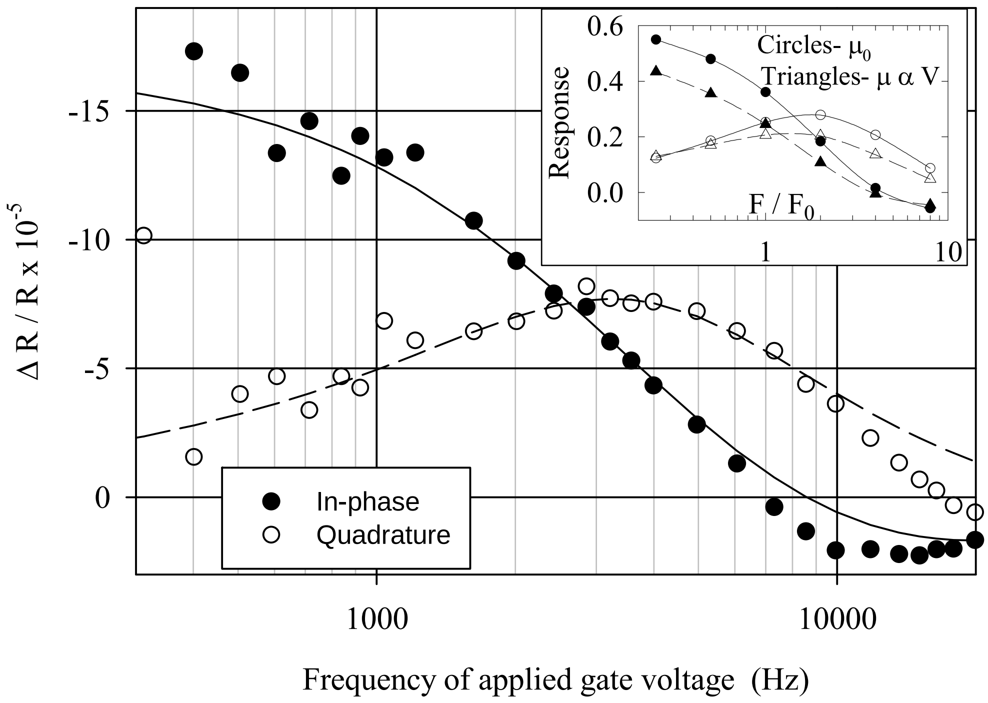

Figure 4.6 Change in reflectance for a sample made with alumina dielectric (TIPS/Al_2O_3 Sample 1) as a function of the gate voltage frequency, V_{gs} = 0 to -100 V. Satisfactory fits to Equation 4.1 were not possible within the error bars using data at all frequencies; the curves show the fits using the F < 6 kHz data only. Inset shows calculations of response for constant mobility (circles) and charge density dependent mobility ($\mu = \mu_0 V(t)/V_{gs0}$) (triangles.)

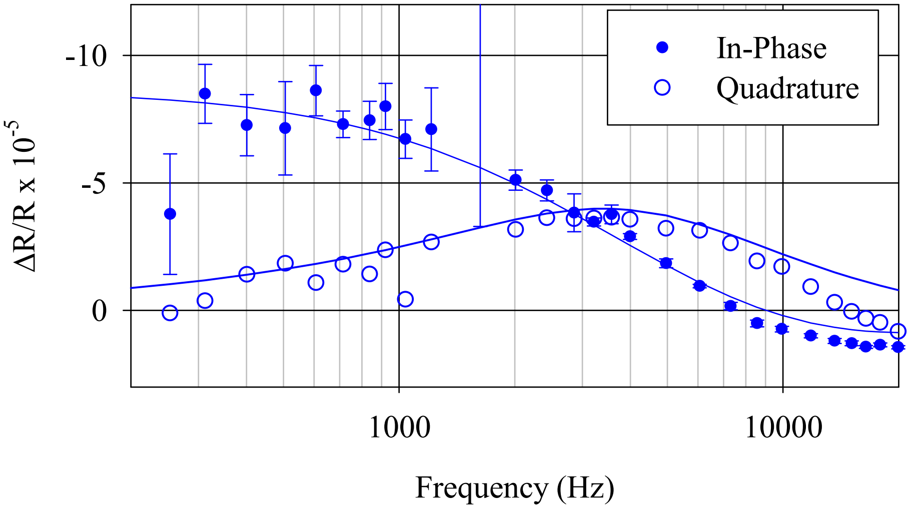

Figure 4.7 Change in reflectance for a sample made with alumina dielectric (TIPS/Al_2O_3 Sample 3) as a function of the gate voltage frequency, V_{gs} = 0 to -50 V; the curves show the fits using the F < 6 kHz data only.

Dielectrics are known to affect the transport properties of organic FETs, due to increased polarization on high ε dielectrics or increased trapping sites. [24,61]. Charge trapping will cause a voltage dependence of the mobility, which causes the mobility to increase as traps are released at higher voltage [18]. In comparing calculations of mobility "dependent" ($\mu \propto V_{gs}$) and "independent" charge density (inset, Figure 4.6), we find that this cannot explain the effects we are seeing. If the mobility was decreasing with voltage (which is not expected from the literature, but applies to our samples, as below) we would see the time dependence of the signal become more like the linear response, since charge bottlenecks at the contacts would not occur when $V_{applied} = 0$. However, the linear calculations also do not show a good fit to the data taken on samples with Al_2O_3 dielectric. We may be seeing increased impedance at the contacts, possibly due to defects near the electrodes [45], due to lamination or molecular disorder as diagrammed in Figure 4.8. This would cause delays in both the injection and extraction of charge in the transistor (which may be asymmetric), and has proved difficult to model.

Figure 4.8 Cartoon of possible defects at the drain and source contacts. (a) shows the effects of poor lamination, where at the contacts the crystal is not in contact with the dielectic, and (b) shows disorder at the crystal/contact interface.

4.4.1 Voltage dependence of the mobility for samples with Al_2O_3 dielectric

Using the larger signal gained from using a material with higher ε at high voltage, we can look at a possible extension of the electro-optic mobility measurement: studying the voltage dependence of the mobility. Shown in Figure 4.9 is the frequency dependence of the electro-optic signal for various gate voltages of a TIPS Pn transistor made with Al_2O_3 dielectric (TIPS/Al_2O_3 Sample 1). Table 4.2 compares the mobility values obtained from fitting the electro-optic data to Equation 4.3 and IV data in Figure 4.5. Values of the mobility decrease with increasing voltage, showing the opposite of what has been observed for voltage dependence of the mobility [18].

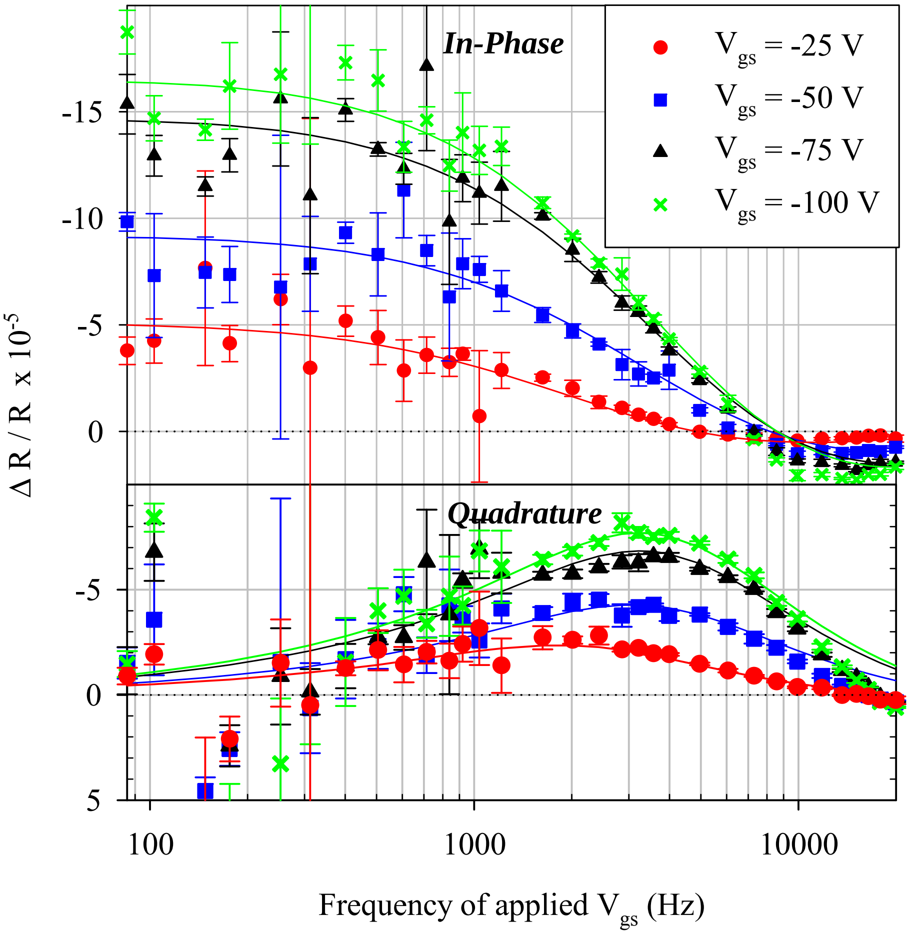

Figure 4.9 Voltage dependence of electro-optic frequency response of TIPS/Al_2O_3 Sample 1.

Table 4.2 Mobility values comparing data presented in Figures 4.5 and 4.9 for sample TIPS/Al_2O_3 Sample 1.

V_{gs}	Mobility (linear)	Mobility from optical data
-25	0.058	0.076
-50	0.036	0.065
-75	0.027	0.046
-100	0.021	0.034

4.5 Mobility variation within a transistor

Transistors grown from drop casting will often form long (~ 1 mm), wide (~ 0.1 mm) crystals, so that multiple “single” crystals can span one pair of drain and source contacts. These crystals often have different transport properties that are compounded in current-voltage measurements. The spatial resolution of our measurement allows us to measure the mobility of individual crystals. Shown in Figure 4.10 are three TIPS Pn crystals grown on the same set of drain and source contacts over PVP dielectric (TIPS/PVP Sample 5.) Figure 4.11 shows the change in reflectance signal as a function of the gate voltage frequency for the three crystals and Table 4.3 gives the mobility for each crystal calculated from fits to Equation 4.2 as well as the linear mobility obtained from current-voltage (IV) measurements (Figure 4.12.)

As seen in the micrograph Figure 4.10, Crystal C is longer (which formed at ~45° off the drain-source gap) and therefore much slower than Crystals A and B (which formed nearly parallel to the drain-source gap.) However the mobility of crystal C is also lower, possibly due to variation in the dielectric material, or due to the anisotropy in TIPS Pn conduction which would result in a factor of ~ 2 decrease in mobility for a crystal oriented at 45° [32]. The compounded mobility of all the crystals calculated from the IV curves is most similar to the mobility of Crystal C, though the width of Crystal C is comparable to A and B and is therefore unlikely to dominate charge conduction. We consider the frequency dependent change in reflectance to be a more reliable measurement of mobility, since it relies on fewer parameters than mobility calculated using IV characteristics, and we therefore attribute the discrepancy to uncertainty (e.g. capacitance, bias stress effects) in the IV measurement.

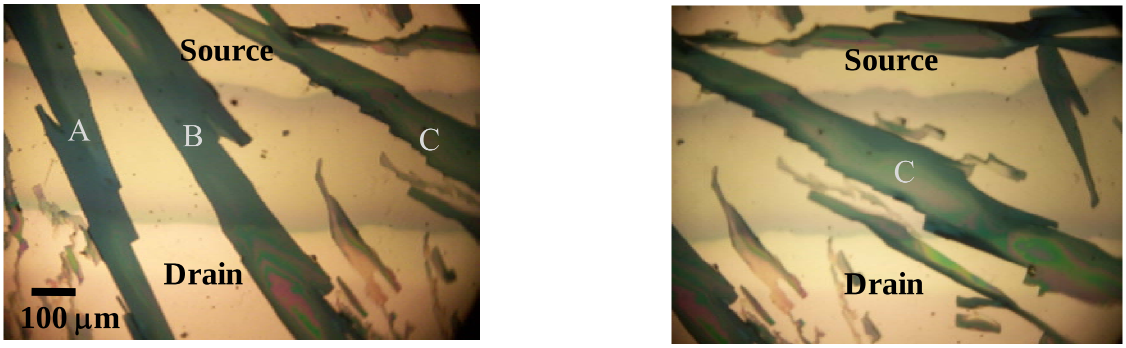

(a) (b)

Figure 4.10 Micrographs of TIPS/PVP Sample 5 with three crystals spanning drain to source. Scale on (a) and (b) are the same, shown as a bar in (a).

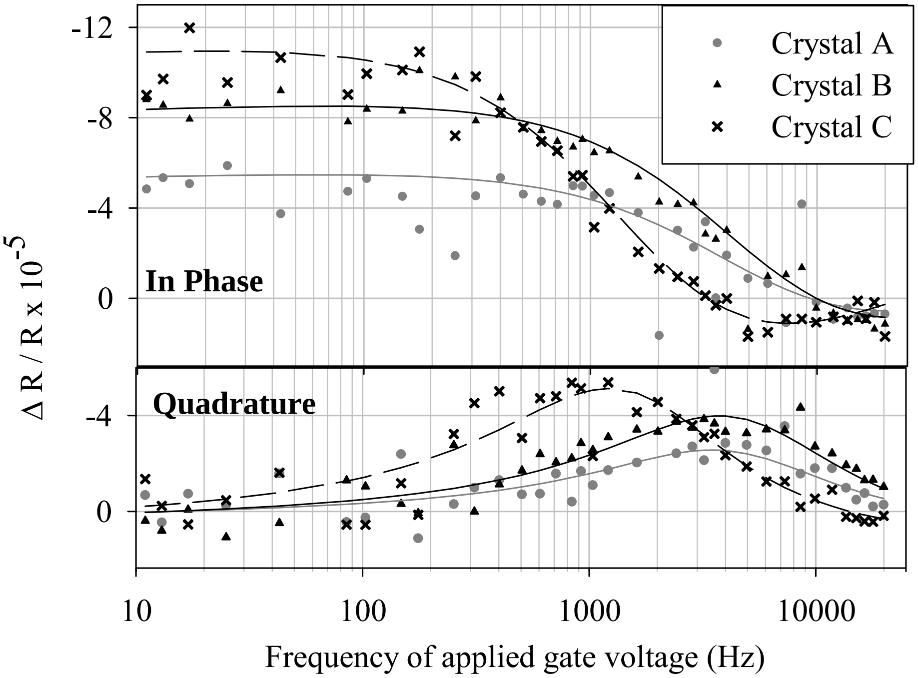

Figure 4.11 Gate voltage frequency dependence of the change in reflectance at the center of a TIPS Pn transistor (TIPS/PVP Sample 5) measured on three crystals spanning one drain-source contact pair, Vgs = 0 to -50 V. Fits (within error bars, not shown to avoid crowding) to Equation 4.1 are shown.

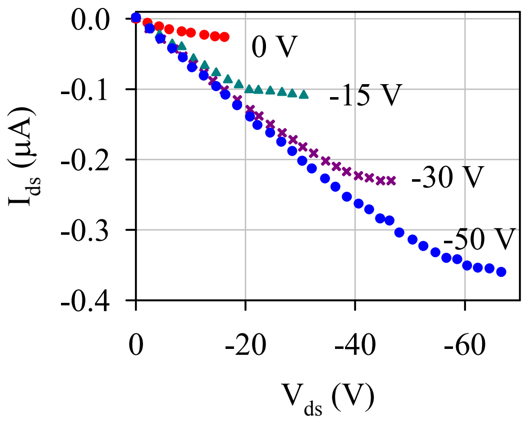

Figure 4.12 Current voltage characteristic for TIPS/PVP Sample 5, gate voltage is labeled.

Table 4.3 Mobilities calculated from the fits to data in Figure 4.11 and from current-voltage (IV) measurements on TIPS/PVP Sample 5. Uncertainty in mobility for crystals A, B, and C are ~20% of the final value, due to uncertainty in V_{gs} (2%), L (5%), and F_0 (10%). F_0 and A are the fitting parameters for Equation 4.1, where the characteristic frequency $F_0 = (\rho_0 V_{gs})/(2L^2)$ and A is the amplitude of $\Delta R/R$.

Crystal	**F_0 (Hz)**	**A (10^{-4})**	**Length(µm)**	**Width (µm)**	**Mobility (cm^2/Vs)**
A	2050	0.9	400	75	0.13
B	2200	1.4	375	125	0.12
C	720	1.8	500	100	0.07
IV	-	-	425 (average)	300	0.07

A similar measurement of the mobility over three crystals on the same transistor for a TIPS Pn sample on Al_2O_3 dielectric is shown below. The frequency dependence of the electro-optic signal (Figure 4.13) shows a similar fit to the data above on Al_2O_3 dielectrics. Comparison between the IV data (Figure 4.14) and electro-optic data is shown in Table 4.4. The electro-optic data in this case shows the difference in mobility between three crystals on the same drain and source contacts, but absolute values of the mobility are more unreliable than for the PVP transistors due to the deviations from the fits at high frequencies.

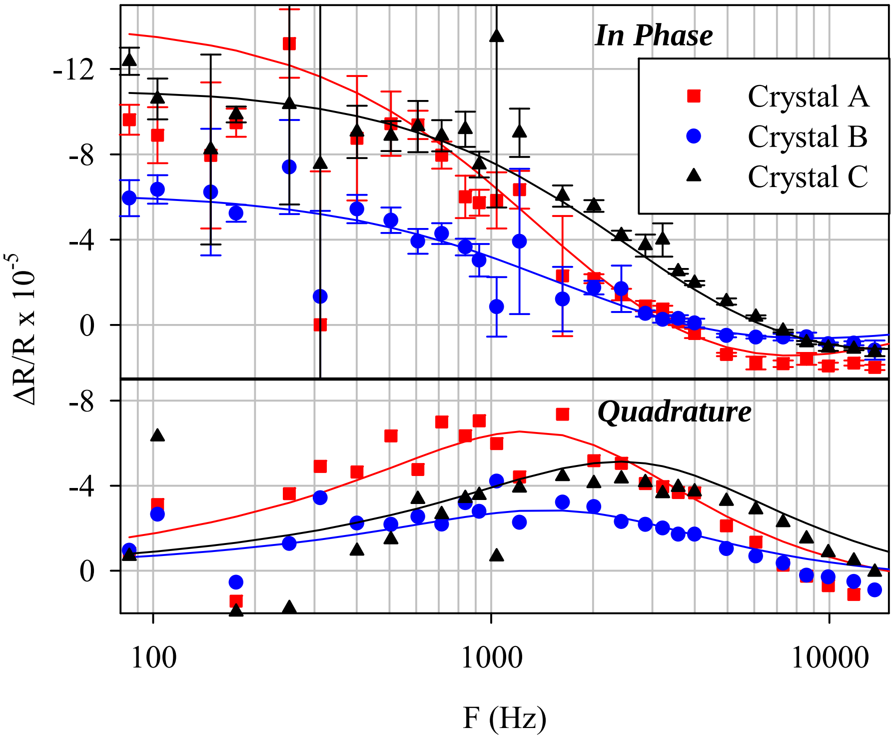

Figure 4.13 Gate voltage frequency dependence of the change in reflectance at the center of a TIPS-pentacene transistor with Al_2O_3 dielectric (TIPS/Al_2O_3 Sample 4) measured on three crystals spanning one drain-source contact pair, Vgs = 0 to -100 V. Fits to Equation 4.1 are shown.

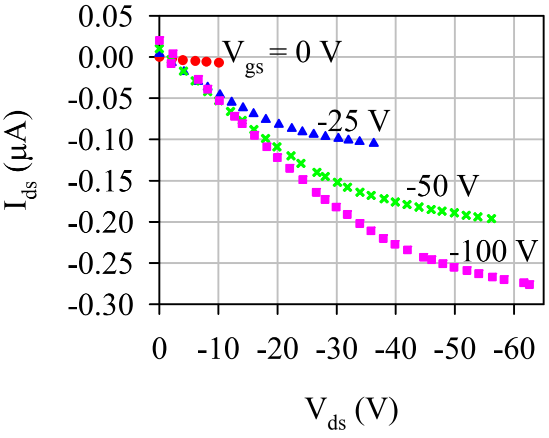

Figure 4.14 Current voltage data for TIPS/Al_2O_3 Sample 4

Table 4.4 Mobility values comparing IV data (Figure 4.14) and electro-optic data (Figure 4.13) of the three crystals on TIPS/Al_2O_3 Sample 4, V_{gs} = -100 V.

Crystal	**F_0 (Hz)**	**A (10^{-4})**	**Length(μm)**	**Width (μm)**	**Mobility (cm^2/Vs)**
A	940	-2.3	275	50	0.014
B	900	-1.0	300	100	0.016
C	1300	-1.8	275	100	0.020
IV	-	-	275	250	0.019

4.6 **Hot spots: areas of locally high ΔR/R signal**

A majority of samples we studied with TIPS Pn as the active layer and PVP dielectric show behavior typical to what is presented in Chapter 3 and Section 4.3. Occasionally we observed a small area with a higher ΔR/R signal, sometimes up to 10 times higher than the rest of the crystal. These areas have been nicknamed "hot spots."

The spatial dependence of the ΔR/R signal is plotted in Figure 4.15 for a sample with a hot spot. The corresponding current-voltage data is plotted in Figure 4.12. As seen, the "normal" (small, negative) signal exists from 0 to 180 microns away from the drain, and at 200 the signal changes to positive and is three times the magnitude. The positive signal persists for ~50 microns, and then returns to the "normal" small negative signal. Most hot spots are smaller than the light spot, which is typically between 20 and 40 microns.

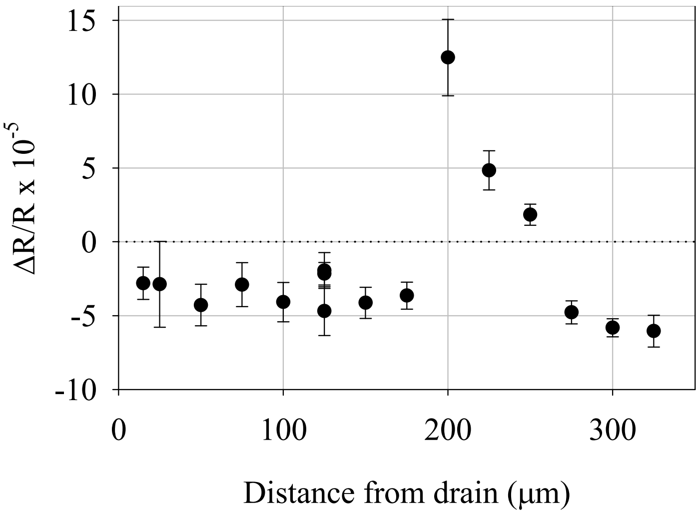

Figure 4.15 Position dependence of the change in reflection signal for a sample with a hot spot, TIPS/PVP Sample 5.

Shown in Figure 4.16 are the voltage modulated spectra for two adjacent (within 20 μm of each other) hot spot areas on another transistor, TIPS/PVP Sample 4, and the voltage dependence of the signals. Hot spot areas may have either increased or decreased reflection, and do not usually form in pairs as in this sample. As seen in Figure 4.16 b, the signal increases quadratically with voltage.

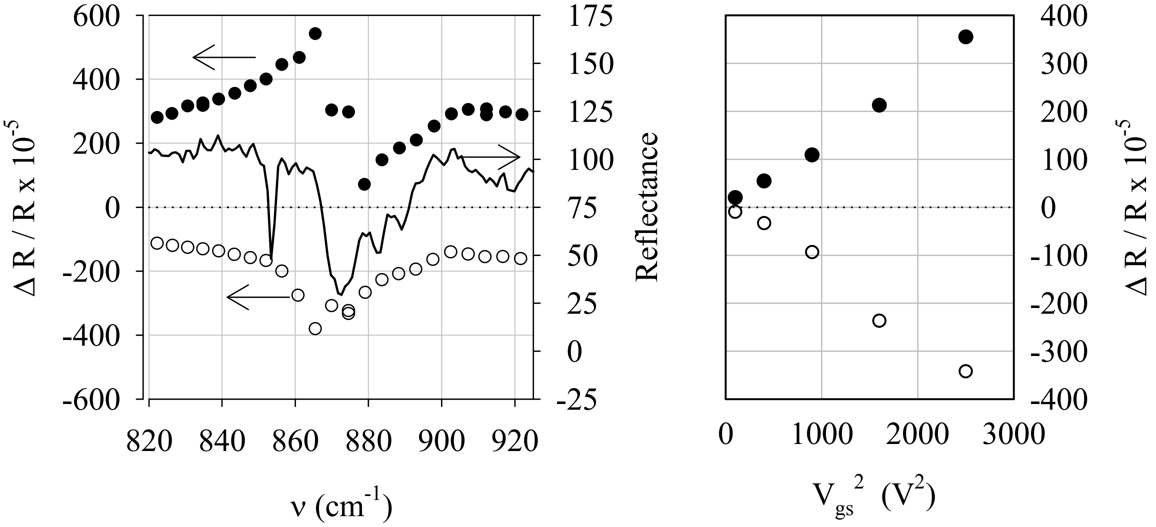

Figure 4.16 Voltage modulated spectrum (a) and voltage dependence of the modulated reflectance spectrum (b) for two hot spots at adjacent positions on TIPS/PVP Sample 4.

The same vibrational mode is affected by the applied voltage in both the increased and decreased reflection areas, though the spectrum of the positive (increased reflection) area is characteristic of a blue shift of the mode, and the spectrum of the negative (decreased reflection) area indicates an increase in the intensity of the mode. Changes in the frequency of the vibrational mode are expected when an electric field is applied, and the changes seen here most likely occur due to large local fields.

The quadratic dependence on voltage suggests that the local charging mechanism may differ from other "typical" areas. However, charge is still flowing on and off these areas through the "normal" parts of the crystal, so the dynamic response is similar to that of a typical sample. A frequency dependence for the hot spot on TIPS/PVP Sample 5 is plotted in Figure 4.17. The position dependence of the signal for this sample is presented in Figure 4.15, and is the same as Crystal A from the first data set in Section 4.5. The hot spot is not exactly centered between the drain and source contacts, but is still close enough that Equation 4.3 can be used to fit the data (as explained in Section 1.6.) For the frequency dependence, the position of the light spot was chosen so that the largest signal could be collected. The mobility from the fit is 0.15 cm^2/Vs, which is within uncertainty of the value measured at the center of Crystal A (Table 4.3.)

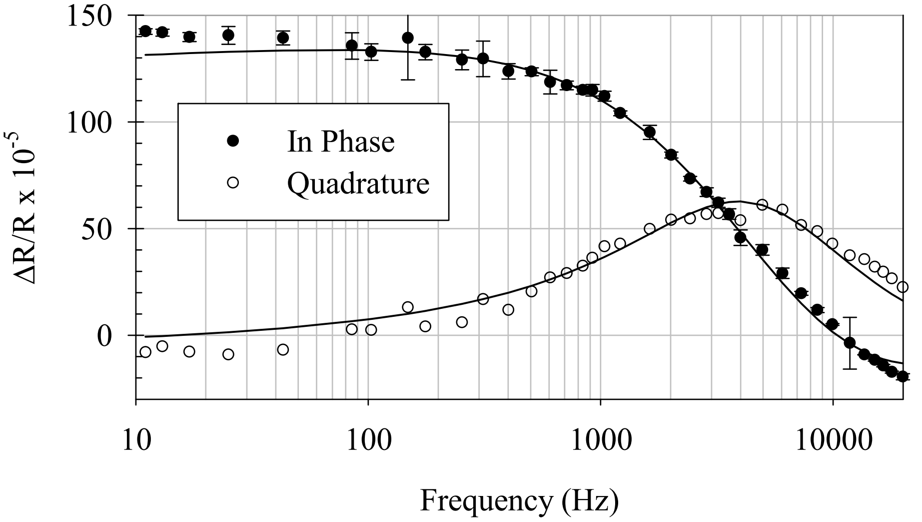

Figure 4.17 Frequency dependence of the hot spot on crystal A of TIPS/PVP Sample 5.

We have not been able to determine whether the high electro-optic signal and extra voltage dependence in these “hot spots” is an optical or a material effect. Areas with large signal first appeared on TIPS Pn samples with very thin (~300nm) PVP dielectric. There were no visible defects in these areas and so we attributed these anomolies to pinholes in the thin dielectric. Later, hot spots were found on samples with thicker PVP layers, and were often associated with visible defects, such as the meeting area between thicker and thinner crystals. Grain boundaries show large voltage drops and charge densities [3,72], and charge trapping by chemical impurities can cause local distortion of the electric field [78,79]. With the spatial resolution of our IR measurements, we may be seeing the effects of local imperfections on the electric field. Unfortunately, the origin of the high signal in these areas remains a mystery.

4.7 Transistors with diF TES ADT

Contrary to measurements on TIPS Pn transistors, those made with diF TES ADT as the OSC did not show a uniform spatial dependence of the ΔR/R signal. As shown in Figure 4.18, the signal was largest at the center of the channel and decreased toward the ends. In FTES/PVP Sample 2, no visible defects existed, whereas in FTES/PVP Sample 1 the surface of the crystal was visibly deformed and seemed to be “bubbled” between 200 and 300 μm. This bubbling was seen on all diF TES ADT samples made at the University of Kentucky, either on or off the transistor. Bubbling of the OSC and the variation in ΔR/R signal are most likely due to the crystal structure transition at 294K as reported by Jurchescu et al. [80]. Between 263-298K, two crystal structures coexist, with the lower temperature structure having a shorter a and b axis (in the plane of the crystal). During crystallization the solvent is being evaporated and can cause the local temperature to be lower than room temperature, causing the lower temperature phase to be a greater fraction of the overall structure upon thin film formation, which then expands and buckles when the high temperature phase becomes dominant at room temperature.

The U shaped position dependence across the transistor is possibly due to the crystal expanding while staying in contact with the drain and source contacts. The crystal most likely expanded while attached at these two points, causing the crystal to bend toward the dielectric. (Figure 4.19) Though the crystals did not lay flat on the substrate, these transistors still retained electronic behavior, meaning that current still flowed through areas not in contact with the substrate (Figure 4.20.) Lower ΔR/R signal at the edges suggests that the channel is charging most where the crystal is in contact, or that the buried metal layer effect is causing a decrease in the signal in areas further than λ/4 from the gate.

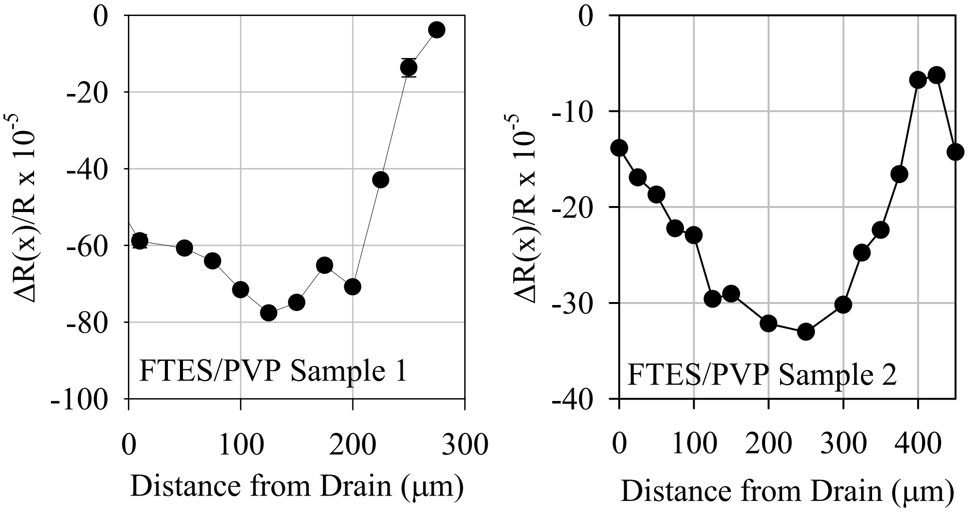

Figure 4.18 Position dependence of the modulated reflectance for two diF TES ADT samples, FTES/PVP Samples 1 and 2.

Figure 4.19 Deformation of diF TES ADT crystals.

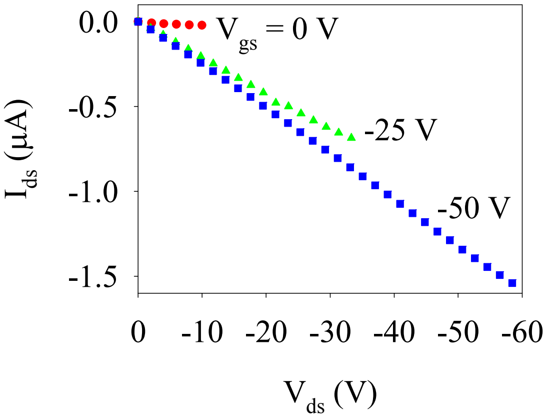

Figure 4.20 Current-voltage data for FTES/PVP Sample 2.

The electro-optic signal as a function of the gate voltage frequency for diF TES ADT 1 is shown in Figure 4.21. Above 3kHz the data deviates from the fit to Equation 4.2, possibly showing the effects of the unusual contact area. The mobility obtained from the fit, 0.17 cm^2/Vs, is ten times lower than the value from current voltage data (Figure 4.20), $\mu_{lin} = 2\ cm^2/Vs$. Degradation of the signal is seen in samples made with diF TES ADT, as discussed in Section 3.2.1, which corresponds to a decrease in the mobility. In the week between IV and frequency dependent measurements (when position and voltage dependence was being measured) the electo-optic signal decreased by 1/3. If the material is "bubbled" at the edge, the characteristic frequency may be much lower than $F_0 = \mu V_{gs}/(2L^2)$ due to increased bottlenecking at the contacts, which is also evident in the drastic decrease in the signal starting at ~ 7 kHz. Due to the unpredictable nature of these samples, further study was not completed.

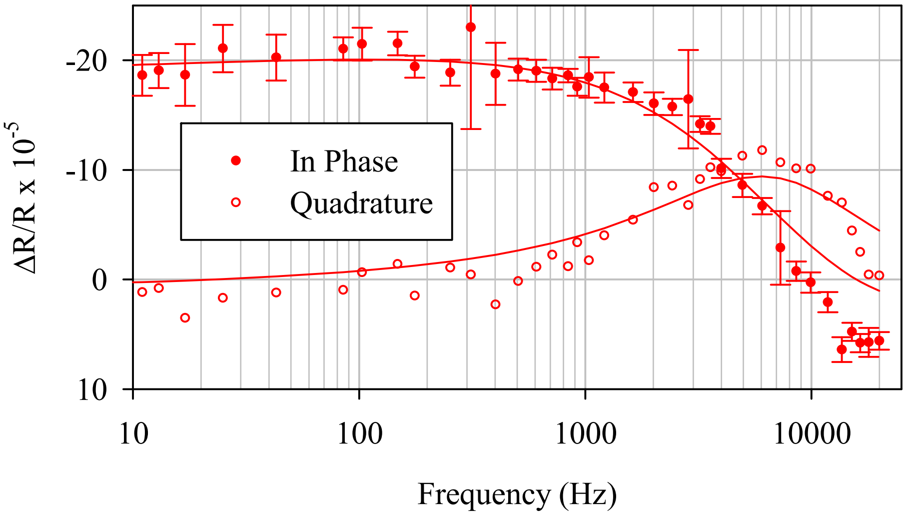

Figure 4.21 Gate voltage frequency dependence of FTES/PVP Sample 2.

4.8 **Summary**

We measured the applied gate voltage frequency dependence of the charge flowing into the center of organic field effect transistors. Fitting this data to a model of a one-dimensional transistor we can obtain accurate values of the mobility. Measurements of TIPS Pn transistors on PVP dielectric fit well to the model, whereas those on alumina dielectric show deviation from the calculated charge density response, suggesting that contact impedance affects the transistor at high frequency.

Individual crystals within one transistor can vary in their transport properties, which are compounded in current-voltage characteristics. Position dependent mobility measurements can be used to probe local areas for mobility. In addition, local measurements of the charge density and dynamics can show unusual behavior of the transistor, as on diF TES ADT samples where problems with semiconductor lamination lead to an effect on the dynamic response, and on “hot spots” on TIPS Pn samples where a localized area shows large signal with quadratic voltage dependence that still retains a dynamic response that fits our simplified model.

CHAPTER 5 **Conclusions**

We used measurements of the voltage modulated infrared reflectance of organic thin film transistors to study the static and dynamic charge in the transistor. The two organic materials studied are soluble, small molecule semiconductors: 6,13 bis(triisopropylsilylethynyl)-pentacene (TIPS Pn) and fluorinated 5,11 bis(triethylsilylethynyl) anthradithiophene (diF TESADT.) Our study showed expected behavior as predicted by a simple model of a one-dimensional conductor, including a reliable measurement of mobility, and also showed deviations from the model due to changes in the dielectric material, imperfections on the transistor, and lamination effects.

In TIPS Pn paired with polymer or aluminum oxide dielectric, a broadband absorption signal is measured for the mid infrared (425 cm^{-1} – 1100cm^{-1} range.) This signal was used to plot the static charge between drain and source and shows a constant value for low applied gate voltage frequencies. When the frequency of the applied voltage is varied, the absorption signal at the center of the gap decreases at the characteristic frequency of the transistor, which is related to the mobility. By fitting the frequency dependent data to the one-dimensional model, we are able to extract the mobility and check for deviations from "ideal" behavior. Mobility values match the values calculated from current-voltage data, and fits show good agreement with data for samples made on polymer dielectric. Samples made on aluminum oxide dielectric show this deviation from the fit at high frequencies (> 6kHz), most likely due to contact impedance effects.

The electro-optic measurement of the mobility only requires information on the length and characteristic frequency of the transistor, and can be used to determine the local mobility. To determine the local mobility within a transistor channel, we use an infrared microscope to focus the light onto areas smaller than the transistor width. More than one crystal can grow on a set of drain and source contacts, and the mobility may vary by a factor of two. The ability to probe local mobility provides insight into the contributions of individual crystals to the total "average" mobility found using current-voltage data.

On select TIPS Pn transistors on polymer dielectric, local areas with large absorption signal are observed. The localization, quadratic voltage dependence, spectral dependence, and frequency dependence of the "hot spot" signals provide contradictory evidence of their origin that has not been resolved.

In diF TES ADT, it was found that although there was a broadband signal similar to that on TIPS Pn, it degraded quickly with time and had an inconsistent spatial distribution. The inconsistent spatial distribution is most likely due to lamination defects observable on diF TES ADT transistors. This lead to unreliable frequency dependent measurements of the absorption signal, and were not useful in determining the mobility. Though dynamic measurements on the polymer dielectric suffered, measurements of voltage modulated Fourier transform infrared (FTIR) spectra on silicon nitride dielectric showed a change in vibrational modes in drop cast (large crystal) transistors, and a broadband absorption and possible infrared active vibrational modes in spin cast (polycrystalline) transistors in the 1000 cm^{-1} – 2000 cm^{-1} range.

The voltage modulated reflection signal provides a useful method to measure the position, voltage and frequency dependence of the high density charged layer in organic field effect transistors. Notably, the dynamic response at the center of the channel provides a local measurement of the mobility that does not require knowledge of the capacitance or charge density.

References

[1] C. D. Dimitrakopoulos and P. R. L. Malenfant, "Organic Thin Film Transistors for Large Area Electronics," *Adv. Mater.*, vol. 14, no. 2, pp. 99-117, 2002.

[2] C. Wang, H. Dong, W. Hu, Y. Liu, and D. Zhu, "Semiconducting pi-Conjugated Systems in Field-Effect Transistors: A Material Odyssey of Organic Electronics," *Chem. Rev.*, vol. 112, p. 2208, 2012.

[3] S. S. Lee, J. M. Mativetsky, M. A. Loth, J. E. Anthony, and W.-L. Loo, "Quantifying Resistances across Nanoscale Low- and High-Angle Interspherulite Boundaries in Solution-Processed Organic Semiconductor Thin Films," *ACS Nano*, vol. 6, p. 9879, 2012.

[4] L. C. Teague et al., "Probing stress effects in single crystal organic transistors by scanning Kelvin probe microscopy," *Appl. Phys. Lett.*, vol. 96, p. 203305, 2010.

[5] H. Matsui and T. Hasegawa, "Visualization of accumulated charge density in operating organic thin-film transistors," *Appl. Phys. Lett.*, vol. 95, p. 223301, 2009.

[6] M. Fischer, M. Dressel, and B. Gompf, "Infrared spectroscopy on the charge accumulation layer in rubrene single crystals," *Appl. Phys. Lett.*, vol. 89, p. 182103, 2006.

[7] Z. Q. Li et al., "Infrared Imaging of the Nanometer-Thick Accumulation Layer in Organic Field-Effect Transistors," *Nano Letters*, vol. 6, no. 2, pp. 224-228, 2006.

[8] T. Manaka, S. Kawashima, and M. Iwamoto, "Charge modulated reflectance topography for probing in-plane carrier distribution in pentacene field-effect transistors," *Appl. Phys. Lett.*, vol. 97, p. 113302, 2010.

[9] J. Jang et al., "Highly Crystalline Soluble Acene Crystal Arrays for Organic Transistors: Mechanism of Crystal Growth During Dip-Coating," *Adv. Funct. Mater.*, vol. 22, pp. 1005-1014, 2012.

[10] A. C. Arias et al., "All jet-printed polymer thin-film transistor active-matrix backplanes," *Appl. Phys. Lett.*, vol. 85, no. 15, pp. 3304-3306, 2004.

[11] A. Azarova et al., "Fabrication of organic thin-film transistors by spray-deposition for low-cost, large-area electronics," *Org. Electron.*, vol. 11, pp. 1960-1965, 2010.

[12] J. E. Anothony, J. S. Brooks, D. L. Eaton, and S. R. Parkin, "Functionalized Pentacene: Improved Electronic Properties from Control of Solid-State Order," *J. Am. Chem. Soc.* , vol. 123, pp. 9482-9483, 2001.

[13] Hagen Klauk, Ed., *Organic Electronics: Materials, Manufacturing and Applications*.: Wiley-VCH Verlag GmbH & Co. KGaA, 2006.

[14] M.E. Gershenson, V. Podzorov, and A. F. Morpurgo, "Colloquium: Electronic transport in single-crystal organic transistors," *Rev. Mod. Phys.*, vol. 78, pp. 973-989, 2006.

[15] S. M. Sze, *Physics of Semiconductor Devices*, Second Edition ed.: John Wiley & Sons, Inc., 1981.

[16] A. D. Meyertholen et al., "Concentration-dependent mobility in organic field-effect transistors probed by infrared spectromicroscopy of the charge density profile,"

Appl. Phys. Lett. , vol. 90, p. 222108, 2007.

[17] M. Koehler and I. Biaggio, "Space-charge and trap filling effects in organic thin film field-effect transistors," *Phys. Rev. B*, vol. 70, p. 045314, 2004.

[18] K. Ryu, I. Kymissis, V. Bulovic, and C. G. Sodini, "Direct Extraction of Mobility in Pentacene OFETs Using C-V and I-V Measurements," *IEEE Electron Device Lett.*, vol. 26, no. 10, pp. 716-718, 2005.

[19] I. G. Lezama and A. F. Morpurgo, "Progress in organic single-crystal field-effect transistors," *MRS Bulletin*, vol. 38, p. 51, 2013.

[20] D. Gamota, *1620 IEEE Standard Test Methods for the Characterization of Organic Transistors and Materials*. New York, 2008.

[21] T. Manaka, F. Liu, M. Weis, and M. Iwamoto, "Studying Transient Carrier Behaviors in Pentacene Field Effect Transistors Using Visualized Electric Field Migration," *J. Phys. Chem. C*, vol. 113, pp. 10279-10284, 2009.

[22] N. Koch et al., "Conjugated organic molecules on metal versus polymer electrodes: Demonstration of a key energy level alignment mechanism," *Appl. Phys. Lett.*, vol. 82, p. 70, 2003.

[23] A. Kahn, N. Koch, and W. Gao, "Electronic Structure and Electrical Properties of Interfaces between Metals and p-Conjugated Molecular Films," *J. Polym Sci Part B: Polym Phys*, vol. 41, pp. 2529-2548, 2003.

[24] Z. Bao and J. J. Locklin, Eds., *Organic Field-Effect Transistors*.: CRC Press, 2007.

[25] S. Z. Bisri, T. Takenobu, T. Takahashi, and Y. Iwasa, "Electron transport in rubrene single-crystal transistors," *Appl. Phys. Lett.*, vol. 96, p. 183304, 2010.

[26] A. Andringa et al., "Localizing trapped charge carriers in NO2 sensors based on organic field-effect transistors," *Appl. Phys. Lett.*, vol. 101, p. 153302, 2012.

[27] Z. Q. Li et al., "Light Quasiparticles Domniate Electronic Transport in Molecular Crystal Field-Effect Transistors," *Phys. Rev. Lett.*, vol. 99, p. 016403, 2007.

[28] T. Sakanoue and Sirringhaus H, "Band-like temperature dependence of mobility in a solution-processed organic semiconductor," *Nature Mater.*, vol. 9, pp. 736-740, 2010.

[29] J. Y. Lee, S. Roth, and Y. W. Park, "Anisotropic field effect mobility in single crystal pentacene," *Appl. Phys. Lett.*, vol. 88, p. 252106, 2006.

[30] V. Coropceanu et al., "Charge Transport in Organic Semiconductors," *Chem. Rev.*, vol. 107, p. 926, 2007.

[31] A. Troisi and G. Orlandi, "Charge-Transport Regime of Crystalline Organic Semiconductors: Diffusion Limited by Thermal Off-Diagonal Electronic Disorder," *Phys. Rev. Lett.*, vol. 96, p. 086601, 2006.

[32] J. Chen, C. K. Tee, M. Shtein, D. C. Martin, and J. Anthony, "Controlled solution deposition and systematic study of charge-transport anisotropy in single crystal and single-crystal textured TIPS pentacene thin films," *Organic Electronics*, vol. 10, no. 4, pp. 696-703, 2009.

[33] O. Ostroverkhova et al., "Anisotropy of transient photoconductivity in functionalized pentacene single crystals," *Appl. Phys. Lett.*, vol. 89, no. 19, p. 192113, 2006.

[34] R. L. Headrick, S. Wo, F. Sansoz, and J. E. Anthony, "Anisotropic mobility in large grain size solution processed organic," *Appl. Phys. Lett.*, vol. 92, p. 063302, 2008.

[35] A. Shehu et al., "Layered Distribution of Charge Carriers in Organic Thin Film Transistors," *Phys. Rev. Lett.*, vol. 104, p. 246602, 2010.

[36] C. Kittel, *Introduction to Solid State Physics*, 8th ed.: John Wiley & Sons, Inc., 2005.

[37] G. Gruner, "The dynamics of charge-density waves," *Rev. Mod. Phys.*, vol. 60, p. 1129, 1988.

[38] M. E. Itkis, B. M. Emerling, and J. W. Brill, "Electrooptical imaging of chargy-density wave phase gradients: polarity and temperature dependence of the phase slip," *Synth. Met.*, vol. 86, p. 1959, 1997.

[39] J. Dumas, C. Schlenker, J. Marcus, and R. Buder, "Nonlinear Conductivity and Noise in the Quasi One-Dimensional Blue Bronze K0.30MoO3," *J. Appl. Phys.*, vol. 50, no. 10, pp. 757 - 760, 1983.

[40] M. E. Itkis, B. M. Emerling, and J. W. Brill, "Experimental studies of the mechanism of the electro-optical effect in blue bronze," *Phys. Rev. B*, vol. 56, pp. 6506 - 6512, 1997.

[41] M. E. Itkis and J. W. Brill, "Electromodulated Infrared Transmission in Blue Bronze," *Phys. Rev. Lett.*, vol. 72, pp. 2049 - 2052, 1994.

[42] L. Ladino, E. G. Bittle, M. Uddin, and J. W. Brill, "Electro-optic search for critical divergence of the charge-density-wave diffusion constant at the onset of depinning," *Phys. Rev. B*, vol. 76, p. 153104, 2007.

[43] J. Lee, S. S. Kim, K. Kim, J. H. Kim, and S. Im, "Correlation between photoelectric and optical absorption spectra of thermally evaporated pentacene films," *Appl. Phys. Lett.*, vol. 84, no. 10, pp. 1701-1703, 2004.

[44] J. D. Jackson, *Classical Electrodynamics*.: John Wiley & Sons, Inc., 1962, p. 224.

[45] T. Li, P. P. Ruden, I. H. Campbell, and D. L. Smith, "Investigation of bottom-contact organic field effect transistors by two-dimensional device modeling," *J. Appl. Phys.*, vol. 93, no. 7, pp. 4017-4022, 2003.

[46] J. Lin, M. Weis, D. Taguchi, T. Manaka, and M. Iwamoto, "Carrier injection and transport in organic field-effect transistor investigated by impedance spectroscopy," *Thin Solid Films*, vol. 518, pp. 448-451, 2009.

[47] G. A. H. Wetzelaer, L. J. A. Koster, and P. W. M. Blom, "Validity of the Einstein Relation in Disordered Organic Semiconductors," *Phys. Rev. Lett.*, vol. 107, p. 066605, 2011.

[48] R. C. Rai, *PhD. Thesis, Electro-optical Studies of Charge-Density-Wave Materials*.: University of Kentucky, 2004.

[49] J. F. Butler and J. O. Sample, "Tunable diode laser instruments," *Cryogenics*, pp. 661-666, 1977.

[50] B. C. Smith, *Fundamentals of Fourier Transform Infrared Spectroscopy*.: CRC Press, Inc., 1996.

[51] Y. Chen et al., "Dynamic character of charge transport parameters in disordered organic semiconductor field-effect transistors," *Phys. Chem. Chem. Phys.*, vol. 14,

pp. 14142-14151, 2012.

[52] C. Bock et al., "Influence of anthracene-2-thiol treatment on the device parameters of pentacene bottom-contact transistors," *Appl. Phys. Lett.*, vol. 91, p. 052110, 2007.

[53] J. Youn et al., "Influence of Thiol Self-Assembled Monolayer Processing on Bottom-Contact Thin-Film Transistors Based on n-Type Organic Semiconductors," *Adv. Func. Mater.*, vol. 22, pp. 1856 - 1869, 2012.

[54] J.-P. Hong et al., "Tuning of Ag work functions by self-assembled monolayers of aromatic thiols for an efficient hole injection for solution processed triisopropylsilylethynyl pentacene organic thin film transistors," *Appl. Phys. Lett.*, vol. 92, p. 143311, 2008.

[55] I. H. Campbell et al., "Controlling Schottky energy barriers in organic electronic devices using self-assembled monolayers," *Phys. Rev. B*, vol. 54, pp. 14321 - 14324, 1996.

[56] D. J. Gundlach, L. Jia, and T. N. Jackson, "Pentacene TFT With Improved Linear Region Characteristics Using Chemically Modified Source and Drain Electrodes," *IEEE Elecron Device Lett.*, vol. 22, no. 12, pp. 571 - 573, 2001.

[57] H. S. Lee et al., "Effect of the Phase States of Self-Assembled Monolayers on Pentacene Growth and Thin-Film Transistor Characteristics," *J. Am. Chem Soc.*, vol. 130, pp. 10556 - 10564, 2008.

[58] H. Yang et al., "Conducting AFM and 2D GIXD Studies on Pentacene Thin Films," *J. Am. Chem. Soc.*, vol. 127, pp. 11542 - 11543, 2005.

[59] S. H. Kim et al., "High-performance solution-processed triisopropylsilylethynyl pentacene transistors and inverters fabricated by using the selective self-organization technique," *Appl. Phys. Lett.*, vol. 93, p. 113306, 2008.

[60] D.J. Gundlach, Y.Y. Lin, T.N. Jackson, S.F. Nelson, and D.G. Schlom, "Pentacene Organic Thin-Film Transistors -- Molecular Ordering and Mobility," *IEEE Electron Device Lett.*, vol. 18, no. 3, pp. 87-89, 1997.

[61] J. Veres, S. Ogier, and G. Lloyd, "Gate Insulators in Organic Field-Effect Transistors," *Chem. Mater.*, vol. 16, p. 4543, 2004.

[62] H. T. Yi, Y. Chen, K. Czelen, and V. Podzorov, "Vacuum Lamination Approach to Fabrication of High-Performance Single-Crystal Organic Field-Effect Transistors," *Adv. Mater.*, vol. 23, no. 48, p. 5807, 2011.

[63] Y. Jang et al., "Influence of the dielectric constant of a polyvinyl phenol insulator on the field-effect mobility of a pentacene-based thin-film transistor," *Appl. Phys. Lett.*, vol. 87, p. 152105, 2005.

[64] N. Tasaltin, D. Sanli, A. Jonas, A. Kiraz, and C. Erkey, "Preparation and characterization of superhydrophobic surfaces based on hexamethyldisilazane-modified nanoporous alumina," *Nanoscale Res. Lett.*, vol. 6, p. 487, 2011.

[65] T.W. Kelley et al., "High-Performance OTFTs Using Surface-Modified Alumina Dielectrics," *J. Phys. Chem. B*, vol. 107, pp. 5877-5881, 2003.

[66] E. D. Palik, Ed., *Handbook of Optical Constants of Solids III*. San Diego, CA: Academic Press, 1998.

[67] M.D. Groner, J.W. Elam, F.H. Fabreguette, and S.M. George, "Electrical

characterization of thin Al2O3 films grown by atomic layer deposition on silicon and various metal substates," *Thin Solid Films*, vol. 413, pp. 186-197, 2002.

[68] R. J. Kline et al., "Controlling the Microstructure of Solution-Processable Small Molecules in Thin-Film Transistors through Substrate Chemistry," *Chem. Mater.* , vol. 23, pp. 1194-1203, 2011.

[69] D. M. Bishop, "Molecular vibrational and rotational motion in static and dynamic electric fields," *Rev. Mod. Phys.*, vol. 62, no. 2, pp. 343 - 373, 1990.

[70] M. Brinkmann et al., "Electronic and Structural Evidences for Charge Transfer and Localization in Iodine-Doped Pentacene," *J. Phys. Chem. A*, vol. 108, p. 8170, 2004.

[71] D. M. Hudgins and L. J. Allamandola, "Infrared Spectroscopy of Matrix-Isolated Polycyclic Aromatic Hydrocarbon Cations. 3. The Polyacenes Anthracene, Tetracene, and Pentacene," *J. Phys. Chem.*, vol. 99, p. 8978, 1995.

[72] X. Li et al., "Electric Field Confinement Effect on Charge Transport in Organic Field-Effect Transistors," *Phys. Rev. Lett.*, vol. 108, no. 6, p. 066601, 2012.

[73] Valeri P. Tolstoy, Irina Chernyshova, and Valeri A. Skryshevsky, *Handbook of Infrared Spectroscopy of Ultrathin Films*.: John Wiley & Sons, 2003.

[74] M. Weis et al., "Grain Boundary Effect on Charge Transport in Pentacene Thin Films," *JJAP*, vol. 50, p. 04DK03, 2011.

[75] C. Sciascia et al., "Sub-Micometer Charge Modulation Microscopy of a High Mobility Polymeric n-Channel Field-Effect Transistor," *Adv. Mater.*, vol. 23, pp. 5086-5090, 2011.

[76] E. G. Bittle, J. W. Brill, and J. E. Anthony, "Electro-optic measurement of carrier mobility in an organic thin-film transistor," *Appl. Phys. Lett.*, vol. 97, p. 013302, 2010.

[77] D. Natali, L. Fumagalli, and M. Sampietro, "Modeling of organic thin film transistors: Effect of contact resistances," *J. Appl. Phys.* , vol. 101, p. 014501, 2007.

[78] L. M. Smieska et al., "Following Chemical Charge Trapping in Pentacene Thin Films by Selective Impurity Doping and Wavelength-Resolved Electric Force Microscopy," *Adv. Func. Mater.*, vol. 22, p. 5096, 2012.

[79] M. J. Jaquith, J. E. Anthony, and J. A. Marohn, "Long-lived charge traps in functionalized pentacene and anthradithiophene studied by time-resolved electric force microscopy," *J. Mater. Chem.*, vol. 19, pp. 6116-6123, 2009.

[80] O. D. Jurchescu et al., "Effects of polymorphism on charge transport in organic semiconductors," *Phys. Rev. B*, vol. 80, p. 085201, 2009.

VITA

Emily Geraldine Bittle

PLACE OF BIRTH

Rochester, New York, United States of America

EDUCATION

M.S. Physics...October 2009
University of Kentucky, Lexington, KY

B.S. Physics .... May 2006
State University of New York College at Geneseo, Geneseo, NY

PROFESSIONAL POSITIONS HELD

Graduate Research Assistant..2007 – present
University of Kentucky, Lexington, KY

Guest Researcher .... February 2011 - May 2011
National Institute of Standards and Technology, Gaithersburg, MD

Laboratory Manual Editor.. 2006 - 2011
University of Kentucky

Teaching Assistant..2006 - 2008
University of Kentucky

Research Intern ....Summer 2006
Laboratory for Laser Energetics, University of Rochester, Rochester, NY

Lab Instructor..2006
SUNY Geneseo

Undergraduate Research 2005-2006
State University of New York College at Geneseo, Geneseo, NY

Undergraduate Research 2003-2004
State University of New York at Buffalo, Buffalo, NY

HONORS

Max Steckler Fellowship 2009-2010, Kentucky Opportunity Fellowship 2009-2010

PUBLICATIONS

J. Nichols, J. Terzic, E. G. Bittle, O. B. Korneta, L. E. DeLong, J. W. Brill, G. Cao, S. S. A. Seo. "Tuning electronic structure via epitaxial strain in Sr_2IrO_4 thin films" Appl. Phys. Lett. 102, 141908 (2013)

E. G. Bittle, J. W. Brill, J. P. Straley. "Dynamic Infrared Electro-Optic Response of Soluble Organic Semiconductors in Thin Film Transistors" MRS Proceedings, 1501 (2013)

E. G. Bittle, J. W. Brill, J. P. Straley. "Dynamics of Charge Flow in the Channel of a Thin-Film Field-Effect Transistor" J. Appl. Phys. 112, 094507 (2012)

E. G. Bittle, J. E. Anthony, J. W. Brill. "Electro-optic Measurement of Carrier Mobility in an Organic Thin-film Transistor" Appl. Phys. Lett. 97, 013302 (2010)

L. Ladino, E. G. Bittle, M. Uddin, J. W. Brill. "Electro-optic Search for Critical Divergence of the Charge Density Wave Diffusion Constant at the Onset of Depinning" Phys. Rev. B 76, 153104 (2007)

A. Sokolow, E. G. Bittle, and S. Sen. "Solitary Wave Train Formation in Hertzian Chains" EPL 77, 24002 (2007)

SOCIETY MEMBERSHIPS

American Physical Society
Materials Research Society and MRS Student Chapter at University of Kentucky